Hydrodynamic forces on high Bond bubbles rising near a vertical wall at moderate Reynolds numbers: An experimental approach

C. Estepa-Cantero[a,c], C. Martínez-Bazán[a,c], R. Bolaños-Jiménez[b,c,*]

[a]*Área de Mecánica de Fluidos, Departamento de Mecánica de Estructuras e Ingeniería Hidráulica, Universidad de Granada, Campus Fuentenueva s/n, 18071, Granada, Spain.*
[b]*Área de Mecánica de Fluidos, Departamento de Ingeniería Mecánica y Minera. Universidad de Jaén. Campus de las Lagunillas, 23071, Jaén, Spain.*
[c]*Andalusian Institute for Earth System Research, Avda. del Mediterráneo s/n, 18006, Granada, Spain.*

Abstract

The optimisation of industrial processes involving bubbly flows requires a deeper understanding of the forces acting on the bubbles, being particularly challenging when they rise in the presence of solid surfaces. The evolution of the drag and lift forces on a bubble rising in a stagnant liquid near a vertical wall is experimentally characterised here by high-speed imaging. The hydrodynamic forces are determined non-intrusively by applying the Kirchhoff equations to the bubble motion, using the experimental evolution of the bubble velocity and geometry. Three different rising regimes are investigated, namely, rectilinear, zigzag, and spiral, where the initial dimensionless initial horizontal wall-bubble distance, L, is varied from $1 \leq L \leq 4$. The three cases, which fall near the transition between regimes, are defined by the Bond and Galilei numbers, $(Bo, Ga) \approx$ (5,60), (4,99), and (10,108), respectively, being the resulting Reynolds numbers, $60 \lesssim Re \lesssim 110$. In all regimes, both the drag and lift forces increase as L decreases, even after the bubble has moved far enough away from the wall. In the rectilinear case, they remain nearly constant as the bubble rises, whereas in the unstable cases, they oscillate at twice the frequency of the bubble trajectory. The drag coefficient reaches its maximum value when the velocity is vertically aligned, while the lift coefficient peaks when the bubble is at its largest lateral distance. These results are of particular interest because, to our knowledge, there are currently no correlations in the literature that can accurately estimate the hydrodynamic forces within this range of parameters and under the influence of a nearby wall. Furthermore, the experimental measurements presented here could be used as a benchmark for more detailed numerical investigations.

Keywords: Bubble dynamics, Bubble rise, Bubble shape, Wall effect, Kirchhoff equations, Drag and Lift forces

*Corresponding author

Email addresses: cestepa@ugr.es (C. Estepa-Cantero), cmbazan@ugr.es (C. Martínez-Bazán), rbolanos@ujaen.es (R. Bolaños-Jiménez)

1. Introduction

The behaviour of single gas bubbles rising in still liquids is crucial for understanding the fundamental physics of two-phase bubbly flows. These flows are ubiquitous in nature and are commonly encountered in various fields, including biotechnological and environmental processes, water treatment, mineral flotation, carbon capture, drag reduction, microplastic scavenging, magma dynamics, and medical applications, among many other uses (Rodríguez-Rodríguez et al., 2015; Cioncolini and Magnini, 2025). Rising isolated bubbles have been extensively studied (see Maxworthy et al., 1996; Magnaudet and Eames, 2000; De Vries et al., 2002; Zenit and Magnaudet, 2008; Legendre et al., 2012; Tripathi et al., 2015; Cano-Lozano et al., 2016; Sharaf et al., 2017; Bonnefis et al., 2023, among others). A key finding of these works is that the bubble path depends on $Bo = \rho g D^2/\sigma$, and $Ga = \rho\sqrt{gD^3}/\mu$, and consequently on the shape of the bubble, characterised by its aspect ratio, χ (with D the volumetric diameter, ρ and μ the density and viscosity of the liquid, σ the surface tension coefficient, and g the gravity acceleration). While spherical bubbles at low-Bo follow straight paths, larger Bo lead to increased χ, unstable wakes, and path instability, promoting zigzag or spiral trajectories (Zenit and Magnaudet, 2008; Cano-Lozano et al., 2016).

However, in real life, bubbles often interact among them or with solid surfaces (Agrawal et al., 2021; Huang et al., 2025), what changes the dynamics of their rise compared to the free-rising case. In the presence of a solid boundary, non-axisymmetric effects govern the interaction between the bubble and the wall. Furthermore, the wake generated behind the bubble plays a crucial role in shaping this interplay in all hydrodynamic regimes, resulting in distinct trajectory patterns depending on the values of the governing parameters Bo and Ga (Takemura and Magnaudet, 2003; Jeong and Park, 2015; Zhang et al., 2020; Yan et al., 2022; Cai et al., 2024; Estepa-Cantero et al., 2024; Shi et al., 2024). In this regard, Estepa-Cantero et al. (2024) experimentally characterised the kinematics of high-Bond bubbles rising at moderate Reynolds numbers near a wall. These bubbles are commonly found in natural and industrial processes, including bioreactor aeration and chemical reactors. They reported that walls do not play a role in promoting path instability but induce wall-normal deviations in the bubble trajectory and vortex shedding. In their range of values of the Bond and Galilei numbers, the presence of a wall causes a net migration of both stable and unstable bubbles away from the wall with the repulsion effect being stronger the closer the wall was initially to the bubble, in agreement with previous theoretical and numerical results (Magnaudet, 2003; Sugiyama and Takemura, 2010; Sugioka and Tsukada, 2015; Zhang et al., 2020; Yan et al., 2022, 2023), and other experimental works (see, for example, Takemura and Magnaudet, 2003; Cai et al., 2024; Jian et al., 2024; Su et al., 2024, and references therein). In fact, Shi et al. (2024) recently obtained numerically that the wall, if sufficiently close to a bubble in the zigzagging regime, induces the main zigzagging plane to be normal to the wall, as experimentally observed by Estepa-Cantero et al. (2024).

The hydrodynamic forces acting on bubbles rising in an unbounded liquid have been extensively analysed in previous work (Magnaudet and Eames, 2000; Magnaudet, 2003; Mougin and Magnaudet, 2006; Shew and Pinton, 2006; Rastello et al., 2011; Bonnefis et al., 2024; Zhu et al., 2025; Cioncolini and Magnini, 2025). These studies have provided fundamental information on the role of vorticity generation, wake instabilities and unsteady forces in bubble dynamics. Early theoretical and numerical models focused on spherical bubbles at low Reynolds numbers, but more recent research in this regard has explored the effects of bubble deformation, path instability, and wake-induced forces at moderate and high Reynolds numbers. However, the literature shows a lack of results concerning the forces acting on deformable bubbles at high Bond numbers and moderate Reynolds numbers, particularly when the effects of a nearby wall are considered. In particular, there is a clear scarcity of experimental data.

Recently, there has been a growing interest in examining the impact of a solid wall on the hydrodynamic forces acting on the rising bubble. Although most of previous studies have focused on theoretical investigations and numerical simulations (Sugioka and Tsukada, 2015; Zhang et al., 2020; Shi et al., 2020, 2024; Shi, 2024), some experimental results can be found (Takemura et al., 2002; Takemura and Magnaudet, 2003; Xiang et al., 2022; Su et al., 2024; Jian et al., 2024). Nevertheless, the latter works are largely focused on nearly spherical bubbles or two-dimensional configurations. In fact, it has been found that the wall modifies the interfacial forces acting on a bubble, changing from attractive to repulsive as the bubble approaches the wall depending on the values of the governing parameters (De Vries et al., 2002; Sugiyama and Takemura, 2010; Shi, 2024; Shi et al., 2024, 2025). At moderate Reynolds numbers, two competing mechanisms govern the interaction between a rising bubble and a vertical wall (Shi et al., 2024; Shi, 2024). On the one hand, an attractive effect caused by the inviscid Bernoulli mechanism, which results from the liquid acceleration in the narrow gap between the bubble and the wall and, on the other hand, a repulsive effect caused by the interaction between the bubble wake and the wall. The prevailing mechanism depends on the value of the control parameters and has been characterised as a function of the Reynolds number and the aspect ratio of the bubble by Shi et al. (2024). The present study aims to improve our understanding of the interaction between a deformable bubble and a nearby wall by experimentally quantifying the local drag and lift forces acting on the bubble surface. This represents a significant step beyond our previous work (Estepa-Cantero et al., 2024), which focused on the kinematics of the problem, namely the characterisation of the bubble path and velocities. Here, by contrast, we focus on the underlying dynamics, providing spatially resolved force measurements that are largely absent in the existing literature, especially for bubbles at high Bond numbers and moderate Reynolds numbers in wall-bounded configurations.

The drag force experienced by a bubble has been reported to increase due to the wall effect, which was recently determined numerically for spherical bubbles by Shi (2024). Their simulations showed that when a bubble is fixed at a certain distance from the wall, the flow in the narrow gap between the bubble and the wall becomes highly sheared, increasing the drag. This increase can be attributed to the stronger velocity gradients imposed by the no-slip condition at the wall, resulting in additional viscous resistance. Furthermore, their study showed that the wall-induced drag enhancement depends on the Reynolds number and the separation distance, with a more pronounced effect observed for smaller bubble-wall gaps. As for the lift force, it has been extensively evaluated for shear flows (Legendre and Magnaudet, 1998; Kurose et al., 2001; Tomiyama et al., 2002; Adoua et al., 2009; Aoyama et al., 2017; Shi et al., 2020; Xu et al., 2021; Hessenkemper et al., 2021; Hidman et al., 2022; Zhang et al., 2025; Zand et al., 2025; Hidman et al., 2025), even combined with the wall effect (Su et al., 2024), showing a dependence on the Reynolds and Bond numbers, or the aspect ratio, and the shear rate. However, the dependence on bubble size was found to exceed that of shear rate at low Morton numbers (Ziegenhein et al., 2018). The picture changes in the presence of a wall because the vorticity generated by the surface of a rising bubble spreads out in the wake and engages the wall surface, creating a net lateral force that can be repulsive or attractive. In this way, the strength and direction of the lift force exerted by the bubble are strongly influenced by the initial distance from the wall and the Reynolds number.

However, the effect of the wall distance on the hydrodynamic forces has not been directly or systematically analysed. This is especially true for deformable bubbles, which are the focus of the present work. Numerous empirical or semi-empirical correlations for drag and lift coefficients as a function of the governing flow parameters can be found in the literature (see Kure et al. 2021; Liu et al. 2024). Nevertheless, most of these correlations are based on experimental or numerical results and apply only to certain conditions, or overlook the wall induction effect and the bubble deformation. Precisely, the absence of appropriate correlations for calculating the hydrodynamic forces constitutes a primary motivation for this work. Although experimental studies of bubble rise near a wall have been conducted, they have mainly focused on the migration and deformation of bubbles under finite Reynolds number conditions (see Estepa-Cantero et al., 2024, and references in), while the forces have hardly been investigated. In this context, our work aims to provide new experimental evidence on this three-dimensional problem. In particular, we propose an experimental approach that enables the measurement of hydrodynamic forces without contaminating the liquid. In the absence of flow field data, these forces are inferred indirectly from the bubble trajectory, and thus measured simultaneously. Our results could enhance our understanding of the mechanisms governing bubble motion, refine existing models, and facilitate systematic numerical simulations of the problem.

This work is structured as follows. Section 2 outlines the problem and describes the theoretical approach. Section 3 provides details on the experimental facility and methodology. An overview of the bubble's kinematics in the three regimes is given in Section 4. Section 5 presents the results, starting with Subsection 5.1, which discusses the bubble velocity and orientation. Then, the bubble inclination and shape are discussed in subsections 5.2 and 5.3, respectively. Subsection 5.4 presents the lift and drag forces calculated using Kirchhoff equations based on the experimental results. Finally, Section 6 summarises the main conclusions of this study.

2. Problem definition and theoretical approach

The problem at hand is sketched in Figs. 1(a)-(b) and consists of an air bubble ascending with velocity $\mathbf{U}^* = v_x^* \, \mathbf{e_x} + v_y^* \, \mathbf{e_y} + v_z^* \, \mathbf{e_z}$ into a stagnant liquid of density ρ, viscosity μ, and surface tension coefficient σ. The terminal velocity of the bubble is v^*, and its equivalent diameter is defined as $D = (6V^*/\pi)^{1/3}$, where V^* is the volume of the bubble. The bubble rises near a vertical wall, being L^* the initial distance from the centroid of the bubble to the wall. A fixed Cartesian reference frame, $\mathbf{x}^* = (x^*, y^*, z^*)$, is used, where x^* is normal to the wall ($x^* > 0$ when the bubble moves away from the wall), y^* parallel to the wall, and z^* points opposite to gravity (see Fig. 1a). At its release, the centroid of the bubble marks the origin $\mathbf{x}^* = 0$. Note that stars indicate dimensional magnitudes, except for the variables used for making dimensionless the rest of the parameters: distance, velocity, and time are made dimensionless with D, gravitational velocity, $\sqrt{gD}$, and gravitational time, $\sqrt{D/g}$, respectively.

After release, the shape and orientation of the rising bubbles are modelled as sketched in Fig 1 (b). For significant surface tension and negligible inertia effects ($We \lesssim 1$), it can be assumed that the bubble surface is restricted to an oblate ellipsoidal shape (Mougin and Magnaudet, 2001, 2002; Shew et al., 2006; Shew and Pinton, 2006; Zawala et al., 2007; Kusuno et al., 2019; Xiang et al., 2022), with major and minor diameters a and c, respectively. Thus, the shape can be characterised by a prescribed aspect ratio, $\chi = a/c > 1$. Moreover, the azimuthal and pitch angles (ϕ and θ, respectively) define the bubble orientation. The azimuthal angle, $\phi = \arctan(v_y/v_x)$, is the angle from the direction $\mathbf{e_x}$ to the horizontal projection of $\mathbf{U}$, v_{xy}. Note that ϕ defines the horizontal motion of the bubble: when $0 < \phi < |\pm 90°|$, the bubble is repelled from the wall ($v_x > 0$), whereas when $|\pm 90°| < \phi < |\pm 180°|$, the motion is attractive to the wall ($v_x < 0$). Moreover, $\phi > 0$ (resp. $\phi < 0$) indicates that the wall-parallel velocity component is positive (resp. negative). The motion is completely normal to the wall ($v_y = 0$) when $\phi = 0$ or $\pm 180°$. The pitch angle, $\theta = \arctan(v_{xy}/v_z)$, where v_{xy} is the horizontal component of the velocity, is the angle between the vertical direction ($\mathbf{e_z}$) and the bubble velocity vector ($\mathbf{U}$). This angle is always positive and defines the inclination of the velocity vector. Because v_z is always positive, $\theta < 90°$. Note that $\theta = 0$ when the velocity vector is completely vertical ($v_x = v_y = 0$), while $\theta \neq 0$ when there is a horizontal component $|v_{xy}| > 0$. In addition, to assess the alignment of the minor axis with the velocity vector, two additional angles are defined, namely α and β, such that $\theta = \alpha + \beta$, with α the angle from $\mathbf{e_z}$ to the direction of the minor axis ($\alpha > 0$) and β the angle from the minor axis to $\mathbf{U}$ (see Fig.1b). As shown later, $\theta < \alpha$, and therefore $\beta < 0$, what implies that the inclination of the minor axis is larger than that of the velocity vector. When $\alpha = 0$, the minor axis is vertical, and when $\beta = 0$, the minor axis is aligned with the velocity vector, that is, $\theta = \alpha$.

The drag and lift forces can be calculated by using the Kirchhoff equations (Lamb, 1924; Mougin and Magnaudet, 2001, 2002; Shew and Pinton, 2006; Kusuno et al., 2019), which can be applied to describe the motion of a bubble of negligible mass rising in a stagnant

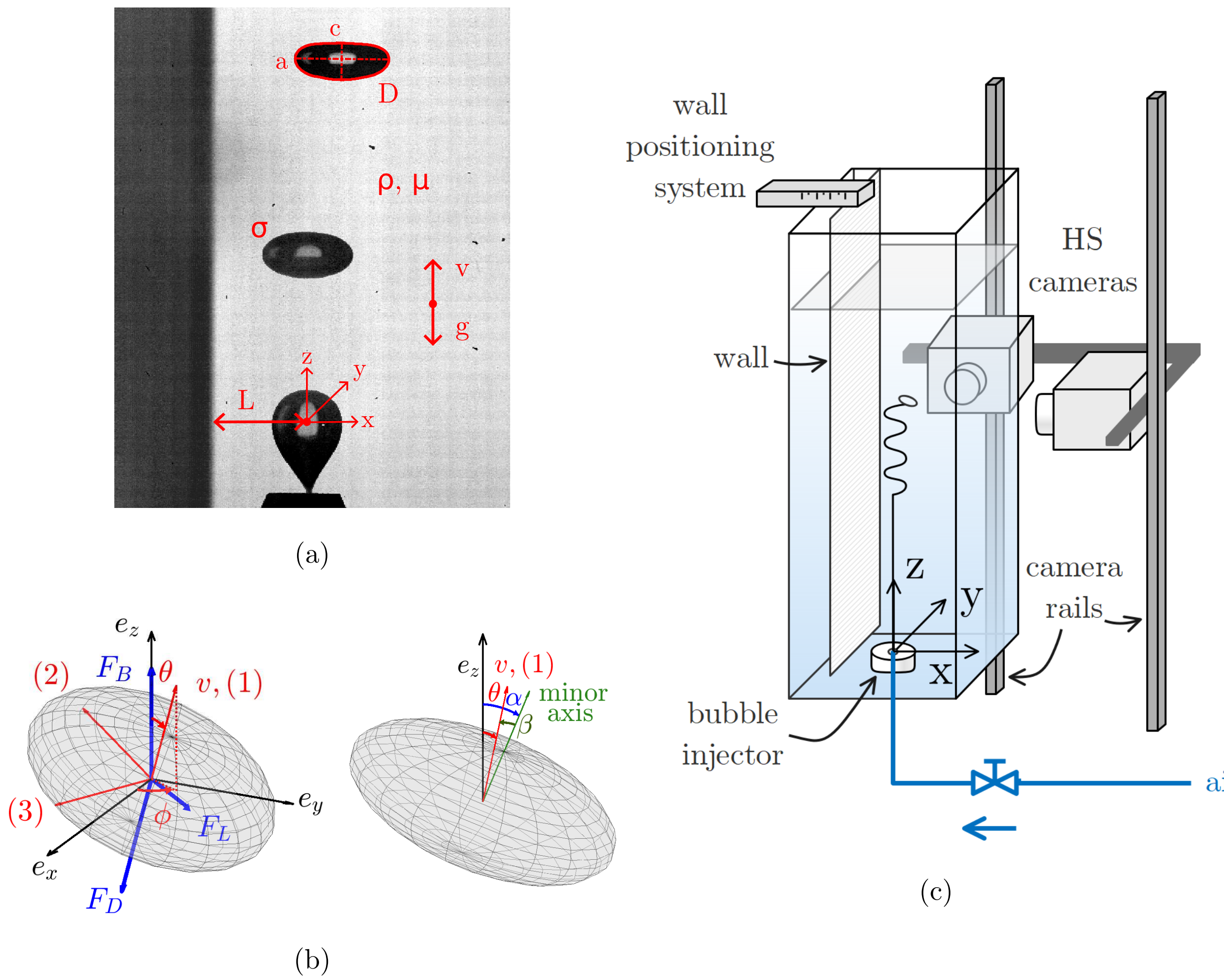

Figure 1: (a) Image of a bubble indicating the main physical and geometric parameters of the problem, together with the major and minor axes of the bubble, a and c, respectively. (b) Sketch of the coordinate system $(1, 2, 3)$ and the forces acting on the bubble (c) Sketch of the experimental facility.

viscous liquid (see Appendix A for more details),

$$\mathbb{A}^* \frac{d\mathbf{U}^*}{dt^*} + \mathbf{\Omega^*} \times (\mathbb{A}^* \mathbf{U}^*) = \mathbf{F}^* = \mathbf{F}^*_\mathbf{D} + \mathbf{F}^*_\mathbf{L} + \mathbf{F}^*_\mathbf{B}, \tag{1}$$

$$\mathbb{D}^* \frac{d\mathbf{\Omega^*}}{dt^*} + \mathbf{\Omega^*} \times (\mathbb{D}^* \, \mathbf{\Omega^*}) + \mathbf{U}^* \times (\mathbb{A}^* \mathbf{U}^*) = \mathbf{\Gamma}^*, \tag{2}$$

where $\mathbf{\Omega^*}$ is the rotation rate of the bubble's centre of mass, $\mathbb{A}^*$ and $\mathbb{D}^*$ are added mass translational and rotational tensors, and $\mathbf{F}^*$ and $\mathbf{\Gamma}^*$ are the resulting hydrodynamic force and torque on the bubble, respectively, being the hydrodynamic force $\mathbf{F}^*$ the sum of the drag, lift, and buoyancy forces ($\mathbf{F}^*_\mathbf{D}, \mathbf{F}^*_\mathbf{L}, \mathbf{F}^*_\mathbf{B}$ respectively). We evaluate Eqs. (1)-(2) in an inertial frame of reference that rotates with the bubble (see Fig. 1b). With the origin O located at the bubble centroid and axes directed along the principal axes of the ellipsoid, we may obtain a diagonal added mass tensor (see Appendix A).

Moreover, we consider that the minor axis c is aligned with the bubble velocity vector ($\beta = 0$), as in previous studies (Shew et al., 2006; Mougin and Magnaudet, 2006; Kusuno et al., 2019), and thus being the inertial frame of reference aligned with directions (1, 2, 3) (see Fig.1b). Direction $\mathbf{e_1}$ points along the velocity vector, $\mathbf{U}^* = U^*\mathbf{e_1}$, and therefore the direction of the drag force. The directions $\mathbf{e_2}$ and $\mathbf{e_3}$ define the plane containing the lift force. In particular, axis 2 is orthogonal to axis 1. The buoyancy force is contained within plane $(1, 2)$, and the positive direction $\mathbf{e_2}$ coincides with the component of the buoyancy force on this axis, F^*_{B2}.

Assuming that $\beta = 0$ allows us to neglect the torque balance ($\mathbf{\Gamma}^* = 0$), and thus Eq. (2) is no longer needed. Under these conditions, the bubble velocity vector has only one component along the direction $\mathbf{e_1}$, $\mathbf{U}^* = U^*_1 = U^*$, and the force components obtained from Eq. (1) simplify to

$$\begin{gathered} F^*_1 = A^*_{11}\frac{\mathrm{d}U^*}{\mathrm{d}t^*} = F^*_D + F^*_{B1}, \\ F^*_2 = A^*_{11}\,\Omega^*_3\,U^* = F^*_{L2} + F^*_{B2}, \\ F^*_3 = -A^*_{11}\,\Omega^*_2\,U^* = F^*_{L3}, \end{gathered} \tag{3}$$

with $F^*_{B1} = \rho g V^* \cos\theta$, $F^*_{B2} = \rho g V^* \sin\theta$ and Ω^*_i the rotation rates in each direction, given by

$$\Omega^*_1 = \frac{\mathrm{d}\phi}{\mathrm{d}t^*}\cos\theta, \quad \Omega^*_2 = \frac{\mathrm{d}\phi}{\mathrm{d}t^*}\sin\theta, \quad \Omega^*_3 = -\frac{\mathrm{d}\theta}{\mathrm{d}t^*}. \tag{4}$$

Note that the force component in direction $\mathbf{e_1}$ depends only on the translation rate, and coincides with the direction of the drag force ($\mathbf{F^*_D} = F^*_{D1} = F^*_D$), whereas the other components depend on the rotation rate. The coefficient $A^*_{11} = C_M \rho V^*$ is the first element of the added mass tensor, with C_M the added mass coefficient, which depends on the shape of the bubble (Lamb, 1924; Tsao and Koch, 1997; Klaseboer et al., 2001). For a spheroidal bubble moving in an unbounded flow (Klaseboer et al., 2001; Zawala et al., 2007; Kusuno et al., 2019) it is defined as

$$C_M = \frac{\gamma}{2-\gamma}, \tag{5}$$

with

$$\gamma = \frac{2\chi^2}{\chi^2 - 1}\left[1 - \frac{1}{\sqrt{\chi^2-1}}\arcsin\left(\sqrt{1-\frac{1}{\chi^2}}\right)\right], \tag{6}$$

being $C_M = 1/2$ for a sphere ($\chi = 1$). Here, we obtain $C_M \simeq 1.49, 1.48$, and 1.74 for the rectilinear, zigzag and spiral regimes, respectively, in agreement with the values obtained for similar bubbles in other studies (Shew et al., 2006). It should be noted that when bubbles move close to a surface, the added mass effect is enhanced (Magnaudet, 2003; Shi et al., 2023). This occurs because the flow in the narrow gap between the bubble and the surface accelerates more significantly than in an unbounded flow. In fact, Milne-Thomson (1996) obtained theoretically that, for a solid sphere moving perpendicularly toward a wall in an ideal fluid, the added mass increases with respect to the unbounded case as the distance to the wall decreases, being the increase of C_M negligible for $L \gtrsim 1$. More precisely, Kharlamov et al. (2008) obtained numerically that $C_M = 0.5 + 0.2182\,(2L)^{-3.21} + 0.081\,(2L)^{-19}$, showing an insignificant increase of C_M for $L \gtrsim 1$. The enhancement of C_M has also been shown to be negligible for deformed bubbles and $L \gtrsim 1$ (Milne-Thomson, 1996; Magnaudet, 2003; Kharlamov et al., 2008; Korotkin, 2008; Xiang et al., 2022; Shi, 2024). Particularly, Zawala and Dabros (2013) obtained that the added mass coefficient corresponding to a bubble approaching a solid wall can be approximated by $C_M = 0.62\chi - 0.12$, that matches for $L \geq 1.25$ and $1 \leq \chi \lesssim 3$ the expression for free flow (Eq. 5). Therefore, since the closest initial distance to the wall in our experiments is $L = 1$, and bubbles immediately migrate away from it, the added mass coefficient for unbounded flow can be assumed in the present study. In fact, the unbounded form of the mass coefficient (Eq. 5) has been applied in previous works on bubbles and drops moving close to surfaces (Tsao and Koch, 1997; Jeong and Park, 2015; Heydari et al., 2022; Cai et al., 2023).

From Eqs. (3), we solve for F_D^*, F_{L2}^* and F_{L3}^*, and considering the definition of drag and lift coefficients, $C_D = 8F_D^*/(\rho\pi D^2 U^{*2})$ and $C_L = 8F_L^*/(\rho\pi D^2 U^{*2})$, respectively, the following expressions are obtained,

$$C_D(t) = \frac{4D}{3U^{*2}}\left(C_M \frac{\mathrm{d}U^*}{\mathrm{d}t^*} - g\cos\theta\right) \tag{7}$$

$$C_{L2}(t) = -\frac{4D}{3U^{*2}}\left(C_M U^* \frac{\mathrm{d}\theta}{\mathrm{d}t^*} + g\sin\theta\right) \tag{8}$$

$$C_{L3}(t) = -\frac{4D}{3U^*} C_M \frac{\mathrm{d}\phi}{\mathrm{d}t^*} \sin\theta. \tag{9}$$

As discussed later, $g\cos\theta \gg C_M \mathrm{d}U^*/\mathrm{d}t^*$, indicating that the drag force must balance the buoyancy force in the direction $\mathbf{e_1}$ ($F_D^* \simeq -F_{B1}^*$). Therefore, F_D^* points to negative $\mathbf{e_1}$ and, according to Eq. (7), C_D must be negative. In addition, $g\sin\theta \gg C_M U^* \mathrm{d}\theta/\mathrm{d}t^*$, implying that F_{L2}^* must balance F_{B2}^*. Thus, F_{L2}^* is directed in the negative direction of axis 2, and C_{L2} must be negative (see Eq. 8). Finally, $C_{L3}(t)$ can be negative or positive depending on the temporal variation of the azimuthal angle: negative if $d\phi/dt^* > 0$ and positive if $d\phi/dt^* < 0$. Note that the characterisation of the bubble shape and orientation, and the evolution of its velocity are required to calculate the force coefficients from eqs. (7)-(9). These values were measured experimentally and are reported below.

3. Experimental setup and methods

The experiments were carried out in an open 1.2 m high tank with a square cross-section of 0.13 m × 0.13 m, as sketched in Fig.1(c). Bubbles were generated by injecting air through an injector at the centre of the tank base. Different injector diameters were used to generate bubbles of varying sizes. In addition, a glass wall was vertically placed inside the tank, whose horizontal position was precisely controlled. The vertical alignment of the entire setup was ensured before every measurement. The reader is referred to Estepa-Cantero

Table 1: Dimensionless parameters governing the three cases considered in this study. All tabulated data are presented as average values ± standard deviation of all experiments for the three regimes.

Case	Regime	L	Bo	Ga	Mo ($\times 10^6$)	Re	We	St
1	Rectilinear	1	5.0±0.2	59.7±1.8	9.87	59.0±0.7	4.99±0.11	-
		2				62.0±0.6	5.49±0.10	
		4				61.6±0.6	5.41±0.08	
2	Planar zigzag	1	3.87±0.03	98.7±0.6	0.61	105.3±2.1	4.72±0.06	0.109±0.004
		2				109.1±0.8	4.89±0.08	
		4				109.1±0.4	4.90±0.04	
3	Spiral	1	10.29±0.15	108±8	8.4±2.3	90.4±0.6	7.96±0.04	0.132±0.006
		2				90.0±0.6	7.90±0.09	
		4				87.5±0.6	7.50±0.10	

et al. (2024) for details of the facility although a brief description is provided in Appendix B.

To study the ascent of the bubble, two high-speed cameras (Photron Fastcam SA1.1, Fastcam Mini Ax200) mounted on a vertical rail were placed perpendicular to each other to record the bubble as it moved. Both cameras were synchronised with a servomotor that controlled the movement if the rail. The servomotor software enabled us to determine the z-coordinate with an accuracy of 1 μm. A laser and photodiode sensor were used to detect bubble pinch-off and trigger cameras recording and motion. Two LED panels provided uniform backlighting for both cameras.

In this study, we considered three cases, which are reported in Table 1, each exhibiting different rising paths based on the numerical analysis of a free-rising bubble by Cano-Lozano et al. (2016). These cases correspond to bubbles 22, 19, and 26 in Cano-Lozano's work, showcasing rectilinear (Case 1), planar zigzag (Case 2), and spiral (Case 3) paths when the bubble rises in an unbounded flow, and falling near the transition between regimes. Cases 1 and 2 were performed with silicon oils T11 and T05, respectively (Dow Corning® XIAMETER™, PMX-200), whereas a mixture of glycerol and water (74.16-74.89% in weight of glycerol) was used in Case 3. The properties of the liquids are described in Estepa-Cantero et al. (2024) and are given in Table B.4. Special care was taken to avoid contamination of the fluids, which were frequently replaced. In fact, the terminal velocities of the bubbles agree with the correlations reported in the literature for clean bubbles.

The captured images were processed using a custom image-based processing routine in Matlab to identify the contour and centroid of the bubbles (see red contour in Fig.1a). The contours were used to determine the size, shape (minor and major diameters), and equivalent diameter of the bubbles, while the centroid position was used to track their paths. Since the directly measured variables were the bubble edge and centroid, the experimental uncertainty depended on the temporal and spatial resolution of the recordings, which ranged from 500 to 2000 frames per second and between 17.79 and 36.31 μm/pixel, respectively. The absolute errors mentioned throughout the manuscript represent the standard deviations among the

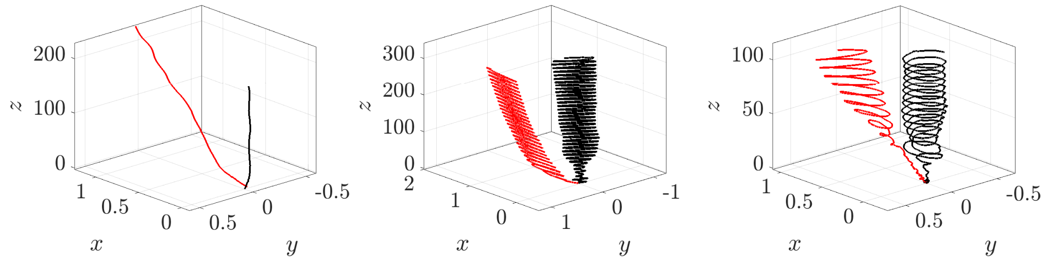

Figure 2: Comparison of the typical trajectories performed by the bubbles in the regimes studied in this work (a) rectilinear, (b) planar zigzag, and (c) spiral with a wall placed at $L = 1$ (red lines) with those without the wall, $L \to \infty$, (black lines). For $L = 1$, the wall is at $x = -1$ along the plane (y, z).

repetitions of each experimental case, which proved larger than the propagated errors from the direct measurements, and a thorough description of the maximum propagated errors is given in Appendix B.

The problem at hand is defined by Bond, $Bo = \rho g D^2/\sigma$, and Galilei, $Ga = \rho\sqrt{gD^3}/\mu$, numbers, together with the dimensionless initial horizontal distance between the centroid of the bubble and the solid wall, $L = L^*/D$. The Morton number, $Mo = g\mu^4/\rho\sigma^3 = Bo^3/Ga^4$, is also used here because it depends only on the liquid properties. Our experiments involved three values of the dimensionless initial wall distance, namely $L = 1$, 2, and 4. Moreover, the results of the problem are defined in terms of Reynolds, $Re = \rho v^* D/\mu = Ga\, v$ and Weber $We = \rho v^{*2} D/\sigma = Bo\, v^2 = Bo\,(Re/Ga)^2$ numbers, with $v = v^*/\sqrt{gD} = Fr = Re/Ga$ the dimensionless terminal velocity of the bubble. In addition, the oscillation frequency in the unstable cases is characterised by the Strouhal number, $St = fD/v^*$, with f the oscillation frequency. Finally, the magnitude of the forces acting on the bubble F^* will be described using the corresponding force coefficients $C_F = 8F^*/(\rho\pi D^2 U^{*2})$. A steady or terminal drag coefficient can be inferred from the balance between the drag and buoyancy forces, namely $C_D^s = 4/3Bo/We = 4/3Fr^{-2}$. The values of the parameters corresponding to the experiments conducted in this work are summarised in Table 1. The ranges covered in the present work are $5 \lesssim Bo \lesssim 10$, $60 \lesssim Ga \lesssim 100$, $60 \lesssim Re \lesssim 100$, $6 \times 10^{-7} \lesssim Mo \lesssim 10^{-5}$ and $4 \lesssim We \lesssim 8$. Under these conditions (intermediate Re and $We \sim 1$) moderate deformations of the bubble surface are expected.

4. Overview of the kinematics of the studied regimes

The bubbles paths were reconstructed using the centroid position over time. The kinematics of the problem was previously studied in Estepa-Cantero et al. (2024) and constitutes the starting point of the work at hand. Thus, this section simply aims to summarise the main features of the three cases studied here:

- Case 1, (Bo, Ga) = (5,59.7), corresponds to stable bubbles rising in the rectilinear regime (Fig. 2a). In this case, when the flow is unbounded, the bubble follows a vertical, straight path. The effect of the wall induces migration of the bubble in the direction perpendicular to the surface, which is enhanced by the wall proximity. As a result, the trajectory deviates from a vertical path and moves perpendicularly away from the wall.

- Case 2, (Bo, Ga) = (3.87,98.7), corresponds to unstable bubbles that rise following a zigzag path (Fig. 2b). In the free case, the average path is vertical; however, when the wall is present, it has a migration effect over the average zigzag path. The direction of the zigzag plane is forced normal to the wall if it is sufficiently close to the bubble ($L \lesssim 1$).

- Case 3, (Bo, Ga) = (10.29,108), belongs to unstable bubbles in the spiral regime (Fig. 2c). In the unbounded case, the axis of the spiral path is vertical with an almost circular horizontal projection of the helix. Similar to Cases 1 and 2, the wall promotes a migration effect on the average spiral path. If the wall is sufficiently close, the bubble cannot develop a complete spiral, promoting a more zigzag-like trajectory parallel to the wall that eventually leads to a flattened spiral motion with small amplitude. Moreover, the minor and major axes of the spiralling motion rotate as the bubble rises.

Although in a different manner, in all three regimes, the wall always induces a migration effect on the bubble (see Estepa-Cantero et al., 2024, for more details). In contrast, attraction or bounce effects were never observed in our range of parameters. This is consistent with Shi et al. (2024), who numerically studied the effect of a wall on deformable bubbles. In their work, a critical Bond number of $Bo_c \simeq 1.4$ is obtained for the transition from attractive to repulsive motion for $Ga \gtrsim 50$. In fact, if (Ga, Bo) of cases 1-3 were plotted in their phase diagram (Fig. 2a in Shi et al., 2024), our experiments would lie in the region where repulsion occurs. Concerning global results, the mean values of Re and We are shown in Table 1. Because the bubble terminal velocity decreases as L diminishes in all regimes (Estepa-Cantero et al., 2024), both Re and We are reduced as L decreases. The values of Re obtained in Cases 1 and 2 of the unbounded experiments are consistent with those reported in the experimental study of Bonnefis et al. (2024) for the same values of Bo and Ga in an unbounded flow. In particular, they report values of $Re \approx 60$ for $Bo = 5$ and $Ga = 60$ using silicon oil T11 (our Case 1), and $Re \approx 100$ for $Bo = 4$ and $Ga = 100$ using T05 (our Case 2).

5. Results and discussion

In this section, the bubble velocity and orientation are characterised in subsection 5.1, its inclination and drift angles are reported in subsection 5.2, and the bubble shape is described in subsection 5.3. Finally, the drag and lift forces obtained by combining the Kirchhoff equations (3) with the experimental data are reported in subsection 5.4.

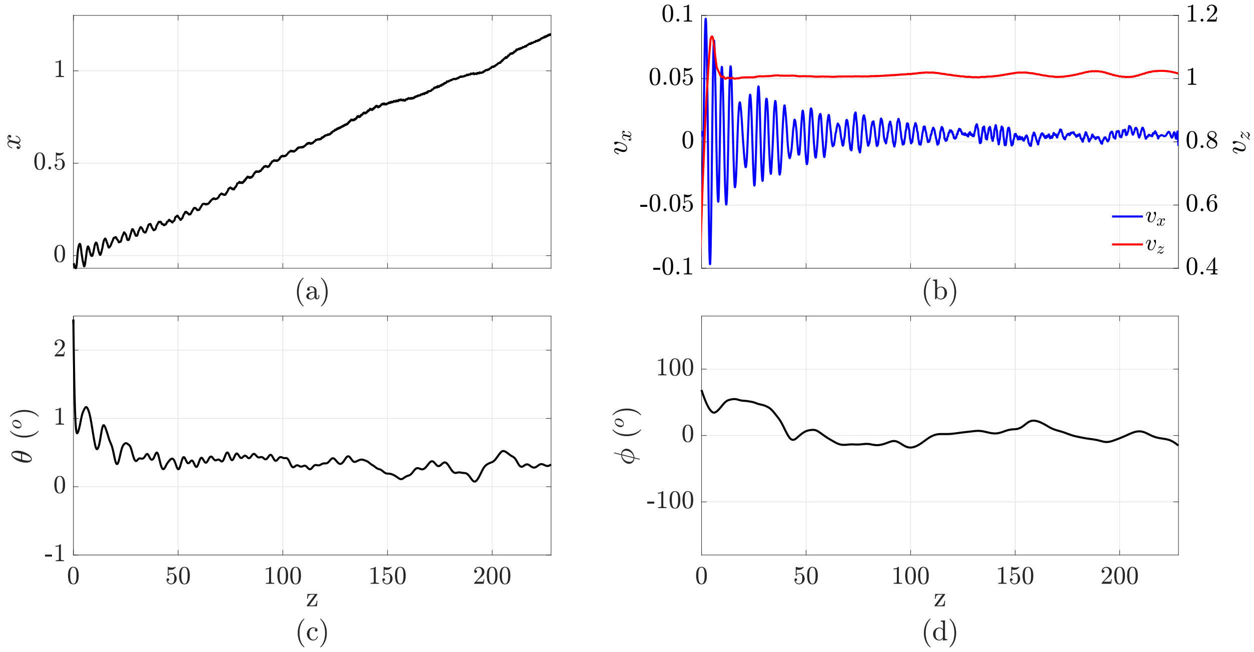

Figure 3: Evolution of the trajectory, velocity, and orientation of the bubble for Case 1 ($Bo = 4.77$, $Ga = 57.6$), and $L = 1$, corresponding to the rectilinear regime. (a) Position of the centroid (wall-normal), (b) components of the velocity of the bubble centroid (wall normal in blue, vertical in red), (c) pitch angle of the velocity vector, (d) azimuthal angle of the velocity vector.

5.1. Bubble velocity and orientation

The trajectories and velocities of the rising bubbles, as well as their pitch and azimuthal angles, θ and ϕ, respectively, were derived from the experimental measurements. The characteristic results for the three cases are shown in Figs. 3-5. In particular, the wall-normal coordinate of the bubble centroid, vertical and transversal velocities, and both θ and ϕ are plotted as a function of the vertical position of the bubble. Only the case corresponding to the closest initial wall distance ($L = 1$) is represented because the global behaviour is similar for larger wall distances.

Case 1

In Case 1 (Fig. 3), the wall-normal distance increased almost linearly with the vertical distance (Fig 3a). During the rise, the vertical velocity (red in Fig. 3b) rapidly increases until it reaches the terminal velocity, $v \simeq 1$, while the wall-normal horizontal velocity, v_x, (blue) reaches a low but positive value after some initial oscillations. Since the bubble movement along the plane parallel to the wall (yz) is negligible, and the wall-normal velocity is much lower than the vertical one, $U \simeq v_z$. This fact is confirmed by the evolution of the pitch and azimuthal angles: θ (Fig. 3c) oscillates around a small value, indicating that the velocity vector exhibits a small inclination with respect to the axis z. The average value of θ increases as L decreases due to the lateral migration generated by the wall. Additionally, the azimuthal angle (Fig. 3d) reflects that the horizontal motion is almost normal to the wall: after a first stage where $\phi \gtrsim 50°$ (the bubble migrates with a wall-parallel velocity

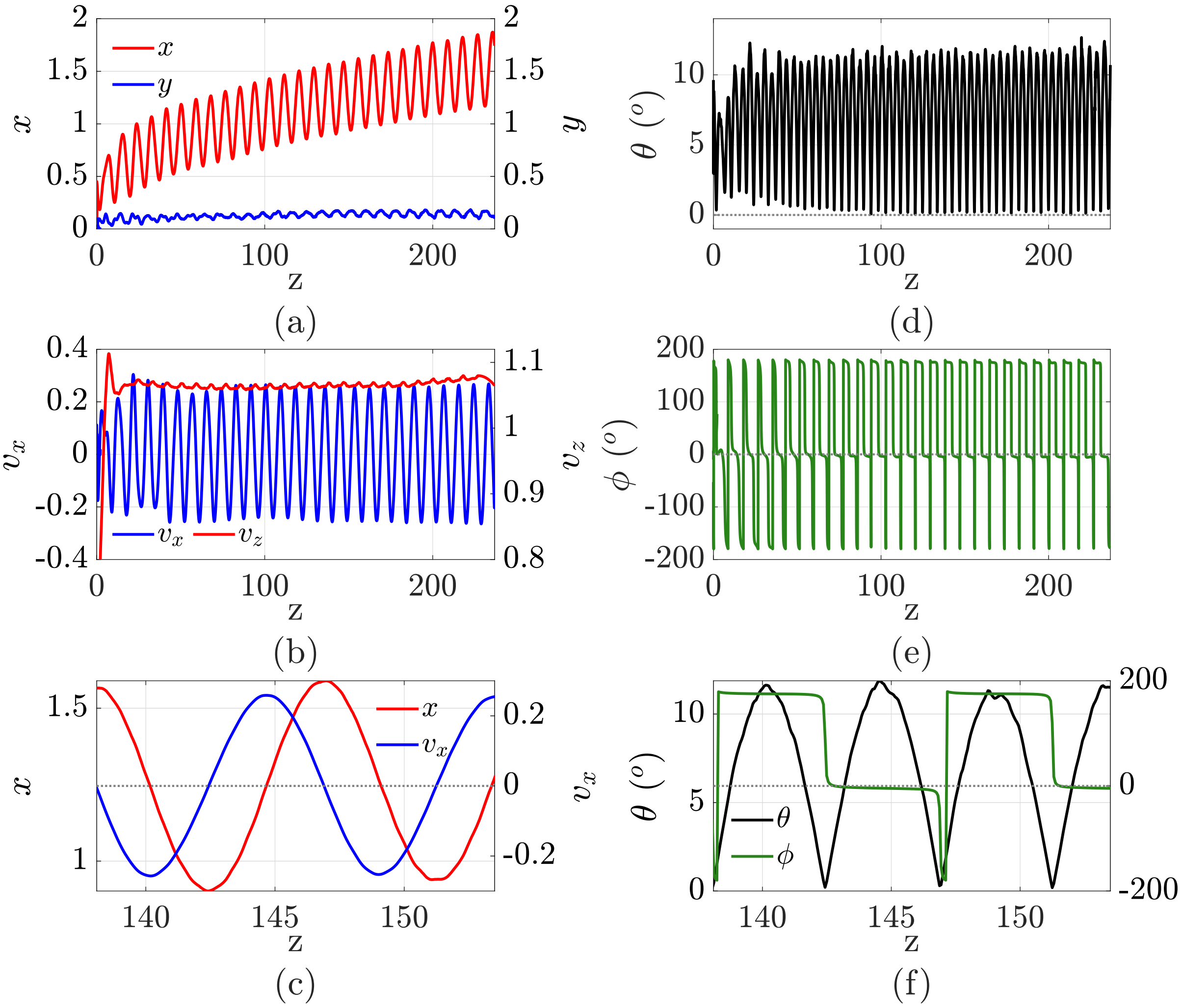

Figure 4: Evolution of the trajectory, velocity, and orientation of the bubble for Case 2 ($Bo = 3.94$, $Ga = 92.7$), and $L = 1$, corresponding to the zigzag regime. Figures on the left show the bubble path and velocity while figures on the right show its orientation angles: (a) position of the centroid (wall-normal in red and parallel in blue); (b) components of the velocity of the bubble centroid (wall normal in blue, vertical in red); (c) detail of $x(z)$ and $v_x(z)$ for $138 < z < 155$ (d) pitch angle of the velocity vector; (e) azimuthal angle of the velocity vector; (f) detail of $\theta(z)$ and $\phi(z)$ for $138 < z < 155$.

component, $v_y > 0$), ϕ drops and, from $z \simeq 50$, oscillates around zero with a small amplitude. This indicates that, although there is a slight motion in the parallel direction of the wall, the horizontal motion occurs mainly perpendicularly to the wall and is always directed away from it ($|\phi| \simeq 0$).

Case 2

For Case 2, shown in Fig. 4, which corresponds to a zigzagging bubble, both centroid coordinates x (blue) and y (red) oscillate as the bubble rises, although the amplitude in x is much larger than that in y (blue) because the main zigzag plane is almost normal to the wall (Fig. 4a). The average value of x increases with z, indicating that the zigzagging motion moves away from the wall. In this regime, the evolution of the vertical velocity (red in Fig. 4b) is similar to that in the rectilinear case, reaching a terminal value $v \simeq 1.1$. Nevertheless, in this case v_z exhibits small-amplitude oscillations with a frequency twice that of the trajectories (Estepa-Cantero et al., 2024), changing the streamwise vorticity sign twice during a zigzag period (Zenit and Magnaudet, 2009; Cano-Lozano et al., 2016). The same terminal velocity was obtained numerically by Shi et al. (2024) under similar conditions ($Bo \simeq 4$, $Ga \simeq 100$) and $L = 1$. In turn, the horizontal velocity in the wall-normal direction (v_x, blue) shows higher oscillations as a consequence of the zigzag motion in which the bubble alternately moves away (increasing x and $v_x > 0$) and towards (decreasing x and $v_x < 0$) the wall during the zigzagging motion, as can be observed in the cycle shown in Fig. 4(c). Although it is an evident outcome, it confirms the validity of our experiments. The vertical velocity is much larger than the horizontal one, so $U \simeq v_z$. The zigzag motion is also reflected in the evolution of the pitch and azimuthal angles. In particular, θ increases cyclically from zero to a maximum value of $\approx 11°$ (Fig. 4d). This indicates that the velocity vector transitions from being entirely vertical ($\theta = 0$) to having a small horizontal component ($\theta > 0$). In fact, the direction of horizontal motion is given by the angle ϕ (Fig. 4e), which oscillates between $\pm 180°$. A closer inspection (see Fig. 4f) shows that $\phi \simeq 175°$ during the approaching stage (decreasing x, see Fig. 4c), while $\phi \simeq -5°$ in the migration phase (increasing x, see Fig. 4b). That is, the horizontal motion is almost normal to the wall with a small component in the wall-parallel direction, in agreement with Fig. 4(a). At the end of the approaching stage ϕ suddenly decreases from $\phi \simeq 175°$ to $\phi \simeq 0$, that is, the bubble turns nearly 180° around the axis z, and the migration stage starts. At the end of this phase, ϕ quickly drops to $\simeq -175°$, that is, the bubble turns nearly 180°. The abrupt growth to $\phi \simeq 175°$ is due to the change of sign of the wall-parallel velocity, v_y. In turn, θ oscillates twice during a zigzagging cycle: $\theta = 0$ at the extreme positions of the trajectory, that is, at the closest and furthest distance from the wall, while the maximum inclination of the velocity vector (maximum θ) occurs at the middle of each stage, when $|v_x|$ is maximum and v_z minimum. The change from the approaching to the migrating phase of the zigzagging motion occurs when $\theta = \phi = 0$, that is, when $\mathbf{U}$ is completely vertical. No significant effects have been found on the frequencies and only a slight change in amplitudes for different values of L, since the bubble moves away from the wall as soon as it is released (Fig. 4a).

Case 3

Regarding Case 3 (Fig. 5a), after a first transient state in which x (red) increases almost linearly and y (blue) remains constant, a spiral is established from $z \simeq 35$. In this case, the path oscillates in both $\mathbf{e_x}$ and $\mathbf{e_y}$ directions. Although a similar amplitude was observed in both coordinates, the bubble motion is not parallel to $\mathbf{e_x}$ or $\mathbf{e_y}$, but is tilted (see Fig. 2c), with x and y being the projections of the real motion. In any case, the oscillations along x are first larger than those along y, evolving to the opposite situation as the bubble rises due to the rotation of the major and minor axes of the flattened spiral as the bubble rises. Furthermore, the average value of x is always positive and grows as z increases, indicating that the bubble is migrating away from the wall. However, the average value of y is almost

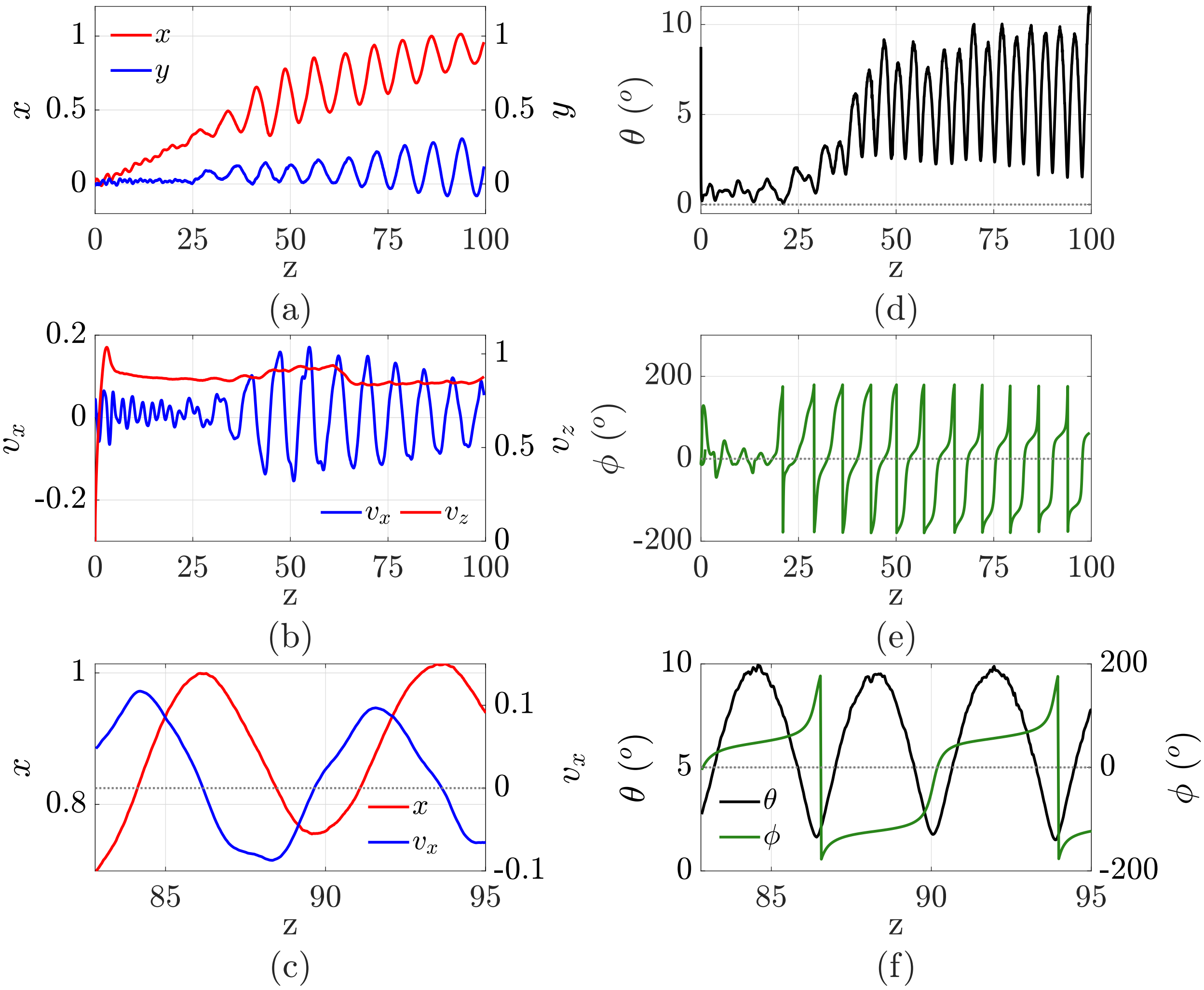

Figure 5: Evolution of the trajectory, velocity, and orientation of the bubble for Case 3 ($Bo = 10.4$, $Ga = 103.5$), and $L = 1$, corresponding to the spiral regime. Figures on the left show the bubble path and velocity while figures on the right show its orientation angles: (a) Position of the centroid (wall-normal in red and parallel in blue); (b) components of the velocity of the bubble centroid (wall normal in blue, vertical in red); (c) detail of $x(z)$ and $v_x(z)$ for $82 < z < 95$; (d) pitch angle of the velocity vector; (e) azimuthal angle of the velocity vector; (f) detail of $\theta(z)$ and $\phi(z)$ for $82 < z < 95$.

zero, which means that no net movement occurs in the wall-parallel direction. As shown in Fig. 5(b), the horizontal wall-normal velocity takes positive and negative values as the bubble moves away from and towards the wall during each cycle of the spiral motion. The amplitude of v_x first increases and then decreases at $z \simeq 70$ because the regime evolves into a more unstable one with higher energy dissipation (Estepa-Cantero et al., 2024; Cano-Lozano et al., 2016). This regime change is reflected in the vertical velocity reduction, which reaches a mean terminal value of $v \simeq 0.85$. The spiralling motion is also observed in the evolution of θ and ϕ: as soon as the spiral regime is established, θ increases twice per cycle from $\theta \approx 0$ to $\theta \simeq 10°$, i.e. the velocity vector changes from vertical to its maximum inclination (see

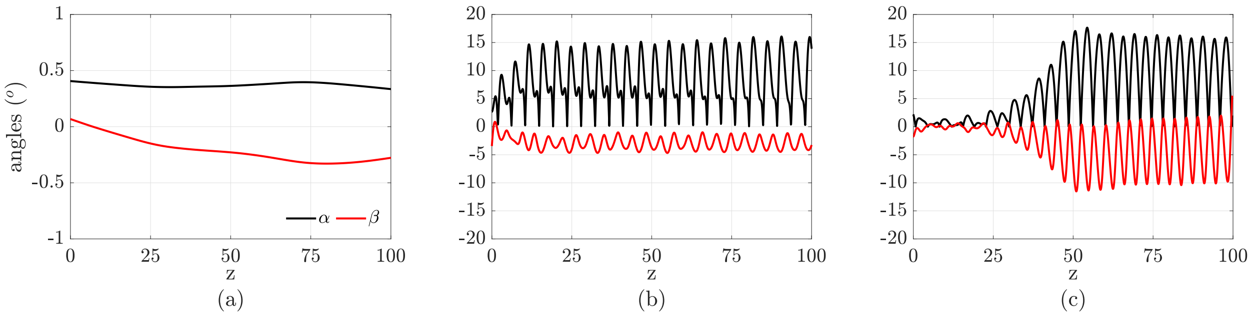

Figure 6: Inclination and drift angles of the bubbles, α and β, respectively, for $L = 1$ in different regimes. (a) Rectilinear regime, $Bo = 4.77$, $Ga = 57.6$; (b) planar zigzagging regime, $Bo = 3.94$, $Ga = 92.7$; (c) spiralling regime, $Bo = 10.4$, $Ga = 103.5$. For clarity, the horizontal axis range is consistent across all cases, although it is truncated in experiments (a) and (b).

Fig. 5d). Conversely, ϕ varies once per cycle over a $\pm 180°$ range (Fig. 5e). If we examine a cycle in Fig. 5(f), it can be observed that during the period the bubble moves away from the wall ($v_x > 0$ in Fig. 5c) ϕ is not zero (unlike in the zigzag regime) because the velocity has a component in the wall-parallel direction. In particular, ϕ gradually increases from $\phi \simeq 40°$ to $\phi \simeq 70°$ during half of a cycle, which corresponds to migration motion with positive v_y. At the end of this stage, the bubble spins and ϕ rises to $\phi \simeq 180°$, which corresponds to wall-normal motion towards the wall ($v_x < 0$ in Fig. 5c). At that moment, ϕ turns negative, increasing from $\phi \simeq -130°$ to $\phi \simeq -100°$, which means that the bubble is approaching the wall ($v_x < 0$, see Fig. 5b) with a negative wall-parallel velocity, $v_y < 0$. Finally, the bubble quickly spins again, ϕ increases until reaching positive values and $\theta = 0$, thereby initiating a new cycle. Since $v_y > 0$ when the bubble migrates from the wall, while $v_y < 0$ when it approaches, in agreement with the path in Fig. 2(c), the velocity vector is directed towards the centre of the spiral, which is consistent with previous studies (Cano-Lozano et al., 2016). As in Case 2, $\theta = \phi = 0$, that is, $v_{xy} = 0$ at the moment of the cycle in which the migration stage shifts to the approaching one. Similar to Case 2, the amplitudes and frequencies were not significantly altered by the wall separation, L.

5.2. *Inclination and drift angles*

Let us now examine the inclination and drift angles, α and β, respectively. Figure 6 shows their typical evolutions over z for the three regimes with $L = 1$. As anticipated, $\alpha > 0$ and $\beta \lessapprox 0$, confirming that the velocity vector is less inclined with respect to the vertical direction than the minor axis (as sketched in Fig. 1b). In the rectilinear regime (Fig. 6a), the absolute value of both angles is very low and nearly constant along the path. Thus, although the bubble migrates from the wall, it remains in the rectilinear regime and rises with a low inclination angle, α. Since β takes very low values, $|\beta| \lesssim 0.3°$, the minor axis is nearly aligned with the bubble velocity vector. This picture changes in Cases 2 and 3 (Fig. 6b,c), corresponding to unstable regimes in which bubbles deviate from a straight path. Thus, the inclination angle, α, varies with time and takes larger values than in Case 1. In particular, in the zigzag case (Fig. 6b) α oscillates around a mean value of $\alpha \approx 7.5°$ with

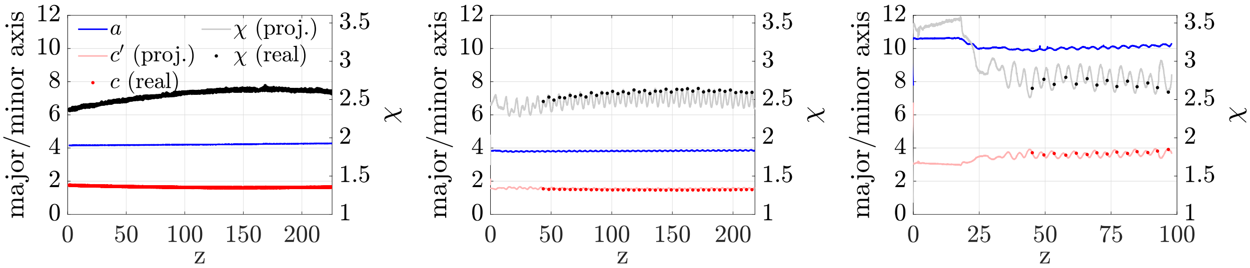

(a) (b) (c)

Figure 7: Downstream evolution of the bubble major and minor diameters and the aspect ratio, χ, for $L = 1$ in the three different regimes. (a) Rectilinear regime, $Bo = 4.77$, $Ga = 57.6$; (b) planar zigzagging regime, $Bo = 3.94$, $Ga = 92.7$; (c) spiralling regime, $Bo = 10.4$, $Ga = 103.5$. The light red and grey lines represent the projection of the minor axis on the vertical plane, c', and the corresponding aspect ratio, respectively. The red and black symbols denote the actual minor diameter and aspect ratio, c and χ, respectively. The left axes represent the minor and major diameters, while the right axes indicate the aspect ratio values.

an amplitude of $\pm 7°$. The drift angle, β, also oscillates but with a lower average ($\approx -2.5°$) and amplitude ($\approx \pm 2°$). Both angles are in anti-phase, indicating that when α increases, β decreases. Although defined differently, an analogous evolution for α and β is observed in the numerical results by Shi et al. (2024) for an equivalent bubble that rises near a vertical wall. Case 3 (Fig. 6c) exhibits a similar picture, in which β oscillates around $-5°$ with an amplitude of approximately $\pm 5°$. The maximum deviation between the minor axis and the velocity vector is always $|\beta| < 10°$ in the three regimes, especially in the zigzagging and in the rectilinear one. Thus, although the minor axis is not strictly aligned with the bubble velocity, $\beta \neq 0$, it can be assumed that $\theta \simeq \alpha$. This fact is somewhat remarkable, as the bubble shapes in this work are notably different from a spherical one, and previous studies (Ern et al., 2012; Cano-Lozano et al., 2016) determined that the bubble inclination is aligned with the path direction only as long as the bubble shape is not too far from the sphere.

5.3. Characterisation of bubble shape

As indicated by Eqs. (7)-(9), to calculate the values of C_D and C_L, in addition to the time evolution of ϕ and θ described above, the added mass coefficient C_M, which depends on $\chi = a/c$ (see Eqs. 5 and 6) is required. Thus, both the major and minor diameters, a and c, must be determined (see Fig. 1a). However, the measurement of the minor diameter c is affected by the inclination of the bubble, which is governed by the angle between the vertical direction and the minor diameter, α. The bubble silhouettes captured by both cameras are indeed projections of the real shape on vertical planes (x, z) and (y, z). Hence, the minor axis extracted from each image, c', corresponds to its vertical projection (Ellingsen and Risso, 2001; Mikaelian et al., 2015), and the actual value of c can only be measured when the minor axis is vertical, that is, when $\alpha = 0$. In this situation, the projection of the minor diameter coincides with its real value, $c' = c$. Consequently, to evaluate the aspect ratio, the minor diameter was extracted from the images where $\alpha \simeq 0$. On the contrary, the major diameter, a, is not influenced by the bubble inclination and can be extracted directly from all the images. Essentially, the same value of a is obtained from the images of both cameras, confirming that the bubble shape is closely approximated by an oblate ellipsoid with a unique major ratio a. Experimental measurements of minor and major diameters are shown in Fig. 7. Note that the real values of the minor diameter (red symbols), extracted when $\alpha = 0$, differ from those measured when the bubble is tilted (light red lines) in unstable regimes.

Similarly, the bubble volume V, which is required to calculate the equivalent diameter D, is also affected by the inclination angle, α. The top view of the bubble is missing; thus, we approximate the volume by integrating slices of the projected area of 1-pixel height in $\mathbf{e_z}$. In this way, using the projection of the bubble shape in both (x, z) and (y, z) planes, at each vertical position z, a horizontal ellipsoidal shape with diameters $d_x(z)$ and $d_y(z)$ is assumed

$$V(z) = \frac{\pi}{4} \int_{z_{min}}^{z_{max}} d_x(z)\, d_y(z)\, \mathrm{d}z. \tag{10}$$

Due to the projected area being larger than the real one whenever $\alpha \neq 0$, the instants where $\alpha = 0$ were isolated to determine the actual volume. For validation, the bubble volume was compared to the initial volume, computed when the bubble was still almost spherical, obtaining an excellent agreement. In addition, an increase in the volume of the bubble with z was observed, which can be explained by the expansion of the air due to the pressure reduction as the bubble rises vertically in the liquid tank: the increase of the bubble volume was 3 to 7%, in excellent accordance with the expected expansion due to the decrease of hydrostatic pressure (8-10% increase of volume per meter of liquid column, depending on the liquid density).

Let us now explore the particular shape of the bubble in each case. As can be observed in Fig. 7, the local aspect ratio, $\chi(z)$, calculated with the real value of c (black symbols), is nearly constant during the bubble ascent, even in the unstable cases. Thus, an average value, χ, will be used for each experiment. Note that the determination of $\chi(z)$ from projections of the bubble when $\alpha \neq 0$ (grey lines) may lead to erroneous values. Furthermore, we see that χ does not depend on L, since the bubble moves away from the wall after it is released (Estepa-Cantero et al., 2024). The mean values of all experiments in each regime are listed in Table 2. Large departures from the spherical shape were achieved for the three cases, with the most deformed bubbles in Case 3 since it corresponds to the largest Bo and We. Bubble deformation can be mainly determined by the Weber number, and many correlations are reported relating χ to We. One of the most extended one is that proposed by Moore considering the potential theory (Moore, 1959, 1965), which is valid for clean bubbles rising in a uniform flow with $We \sim \mathcal{O}(1)$, high Re, and small Mo: $We = 4\chi_M^{-4/3}(\chi_M^3 + \chi_M - 2)[\chi_M^2 \sec^{-1}(\chi_M) - (\chi_M^2 - 1)^{1/2})]^2(\chi_M^2 - 1)^{-3}$. The expression by Moore predicts $\chi_M \to \infty$ when $We \to 4$, and therefore, overestimates χ for our experimental results. Taylor and Acrivos (1964) proposed another correlation for low viscosity and clean bubbles, $\chi_T = 1 + 5/32\, We + \mathcal{O}(We^2)$. Supported by the theoretical results of Blanco and Magnaudet (1995), Rastello et al. (2011) expanded the result by Moore for $We \lesssim 6$ and

Table 2: Mean absolute values of the magnitudes of the aspect ratios and the drag and lift coefficients obtained for the three cases and different wall distances, together with the stationary drag coefficient, C_D^s. All tabulated data refer to the mean value ± standard deviation of all experiments performed for the cases defined by each row and column. Note that the values of χ represent averages over all wall distances.

Case		$L=1$	$L=2$	$L=4$
1	χ		2.53±0.06	
	C_D^s	1.28±0.03	1.17±0.02	1.20±0.01
	C_D	1.29±0.02	1.18±0.02	1.19±0.01
	C_L	0.0088±0.0006	0.0044±0.0002	0.0039±0.0008
2	χ		2.57±0.09	
	C_D^s	1.34±0.10	1.22±0.02	1.21±0.01
	C_D	1.13±0.01	1.07±0.02	1.06±0.01
	C_L	0.143±0.003	0.132±0.006	0.128±0.004
3	χ		2.97±0.17	
	C_D^s	1.74±0.01	1.76±0.02	1.84±0.03
	C_D	1.83±0.04	1.84±0.05	1.79±0.06
	C_L	0.19±0.02	0.19±0.01	0.16±0.03

small Re, suggesting $\chi_R = 1+9/64\,We+3/250We^2+\mathcal{O}(We^3)$ for different liquids. However, the exact shape of the bubble depends not only on We, but also on Re or Mo. In this regard, Legendre et al. (2012) obtained $\chi = 1/(1-9/64\,We)$ for bubbles that rise in different types of water, which is finally corrected with Mo, as $\chi_L = 1/[1-9/64\,We(1+K(Mo)\,We)^{-1}]$, with $K(Mo) = 0.2Mo^{1/10}$. The results of the previous expressions are plotted in Fig. 8 with our experimental values. The predicted aspect ratio for the different correlations strongly increases with We due to surface tension effects becoming less important. In general, χ_L showed the closest agreement with our experiments.

In particular, for Case 1, as reported in Table 2, an average experimental value of $\chi = 2.53$ is obtained for the rectilinear regime, regardless of the initial wall distance. This value is reasonably well predicted by the correlation given in Legendre et al. (2012) (see Fig.8a), which yields $\chi_L = 2.31$, 2.35, and 2.15 for $L = 4$, 2, and 1 respectively, using the corresponding We for each L and the Morton number of the liquid used in the experiments (see Table 1). However, the remaining correlations significantly underestimate the experimental aspect ratio. Moreover, Cano-Lozano et al. (2013) numerically found that bubbles corresponding to case 1 were indeed stable, but with lower aspect ratios. Specifically, for (Bo, Ga, Re)=(5,50,50), similar to the bubbles in Case 1, they obtained $\chi = 1.88$. These differences may be attributed to the axisymmetric approximation assumption in the simulations. Furthermore, Zenit and Magnaudet (2008) used the same oil (T11) as in Case 1 and reported an aspect ratio $\chi \simeq 2.1$ for bubbles with $Bo = 5$. As far as we are concerned, this is the first reference of bubbles with such high aspect ratios that have been experimentally reported to be stable. In Case 2, an average value of $\chi = 2.57$ was experimentally obtained. As shown in Fig. 8(b), the correlation by Legendre et al. (2012) agreed fairly well with the

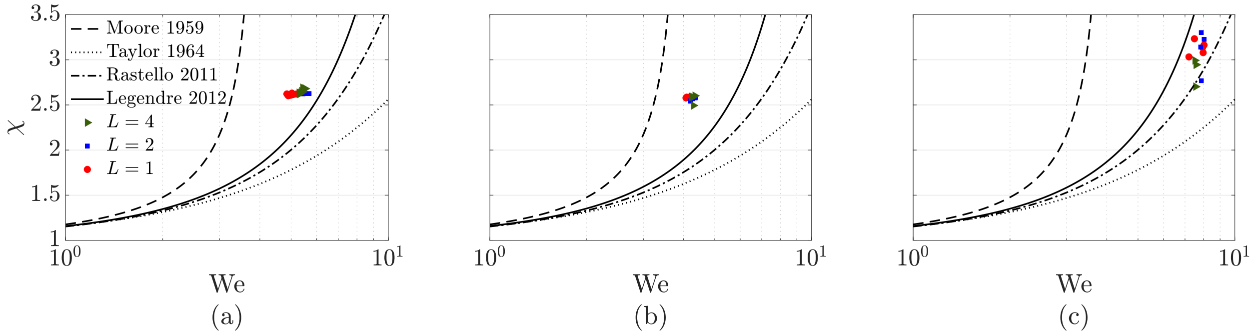

Figure 8: Comparison of the bubble aspect ratio obtained on all the experiments with different correlations in the literature for (a) rectilinear, (b) planar zigzagging, and (c) spiralling regimes. Correlations from Moore (1959); Taylor and Acrivos (1964); Rastello et al. (2011); Legendre et al. (2012).

experimental values, while the rest significantly underestimated the aspect ratio. In particular, $\chi_L = 2.25$, 2.24, and 2.17 for $L = 4,\ 2$, and 1, respectively. The experimental value also agrees with the numerical work by Cano-Lozano et al. (2013), who for (Bo, Ga)=(5,100), obtained an ellipsoidal shape with $\chi = 2.4$. A good qualitative comparison with Shi et al. (2024) is also accomplished, since they calculated an aspect ratio of $\chi \simeq 2.1$ for a bubble in the zigzagging regime with (Bo_S, Ga_S)=(1,30), what corresponds to (Bo, Ga)=(4,85), since $Bo = 4\,Bo_S$ and $Ga = 2^{3/2}\,Ga_S$. Furthermore, our findings are consistent with the experimental results reported by Zenit and Magnaudet (2008), who also reported $\chi \simeq 2.3$ under similar experimental conditions using the same silicon oil. Finally, the highest deformations were observed in Case 3, with an average experimental value of $\chi = 2.97$. In this case, (see Fig. 8c), the experimental results lie between correlations χ_L and χ_R. Legendre et al. (2012) overestimated the experimental result ($\chi_L = 3.51$, 3.86 and 3.92 for $L = 4,\ 2$ and 1, respectively), while Rastello et al. (2011) slightly underestimates the experimental aspect ratio ($\chi_R = 2.73$, 2.86 and 2.88). The average aspect ratio in Case 3 is also similar to the numerical result of Cano-Lozano et al. (2013), who obtained $\chi = 3.19$ for (Bo, Ga)=(10,100) in an unbounded fluid.

5.4. Evolution of local hydrodynamic forces

Assuming that $\beta \simeq 0$, $\chi \simeq$ constant, and C_M is unaffected by the presence of the wall, once the pitch and azimuthal angles, θ and ϕ, the bubble velocity, $\mathbf{U}$, and the aspect ratio, χ, have been determined, the simplified equations (7)-(9) can be used to calculate the drag and lift coefficients. The resulting evolutions of the local values, $C_D(z)$ and $C_L(z)$, are plotted in Figs. 9 and 11, respectively, and the mean values, C_D and C_L, are given in Table 2.

5.4.1. Drag force

The drag coefficient was calculated using Eq. (7). Given that $C_M \sim 1$ and $\mathrm{d}U^*/dt^* \sim 10^{-3}$ m/s^2, the term $C_M \mathrm{d}U^*/dt^* \ll g\cos\theta$, implying that $C_D \simeq -4D/(3U^{*2})\,g\cos\theta$. Since $\theta > 0$, C_D is always negative, indicating that the drag force points to negative $\mathbf{e_1}$ direction, balancing the 1-projection of the buoyancy force in the positive direction ($F_D =$

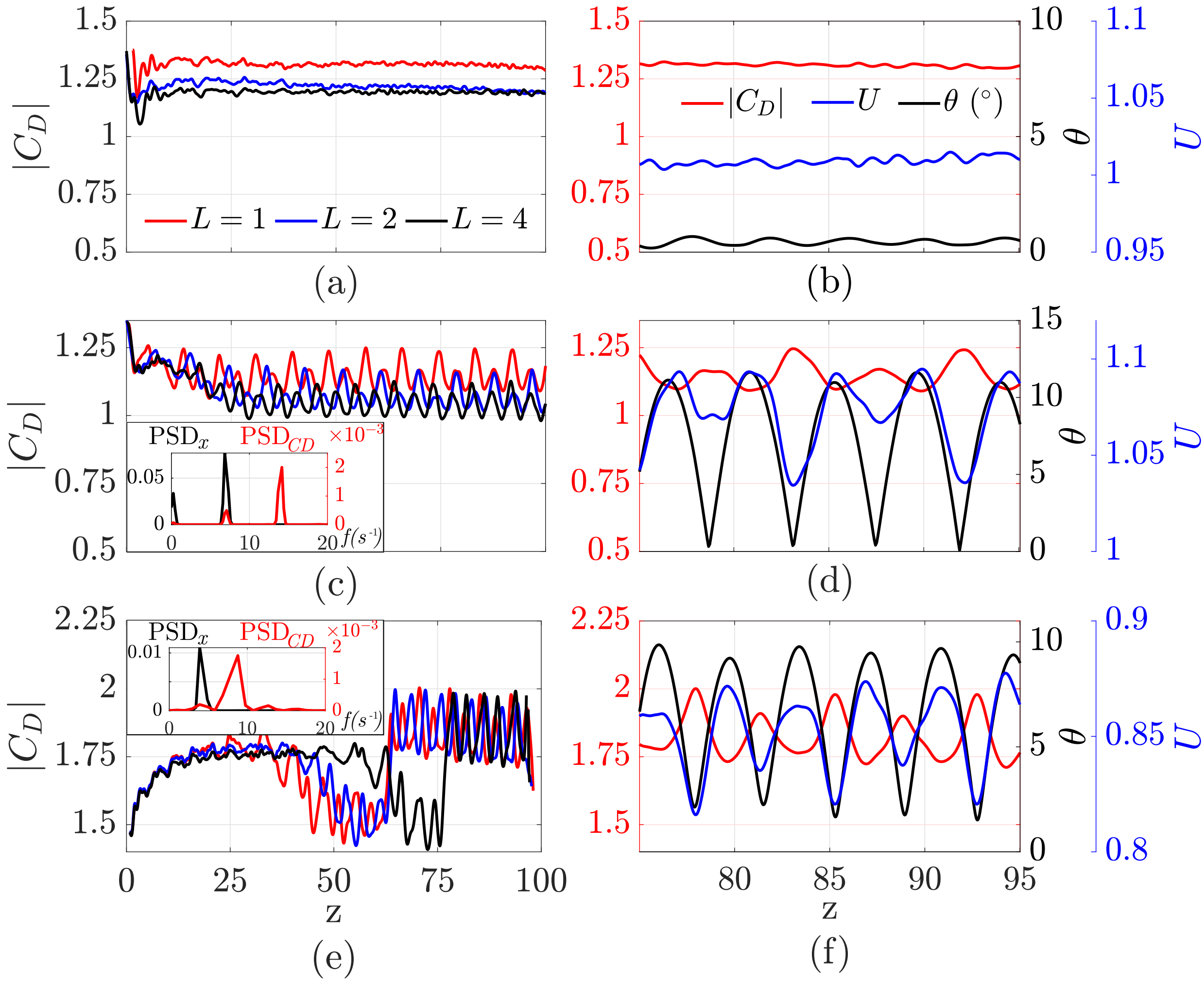

Figure 9: Evolution along the vertical direction of the magnitude of the local drag coefficient, $|C_D(z)|$, corresponding to experiments in the (a, b) rectilinear, (c, d) zigzagging, and (e, f) spiralling regimes, respectively. The left panels show $|C_D(z)|$ for $L = 1$, 2, and 4; including an inset displaying the comparison between the power density espectrum of the oscillating trajectories and that of $|C_D(z)|$. Figures on the right show a zoom of $|C_D(z)|$ (axis on the left) for $L = 1$, together $U(z)$ and $\theta(z)$ (axes on the right in blue and black, respectively). The horizontal axes in Figures (a) and (c) are truncated to $z = 100$ for clarity.

$-F_{B1} = -\rho g V \cos\theta$), in agreement with the sketch in Fig. 1(b). Figure 9 shows the evolution of $|C_D(z)|$ obtained experimentally along the vertical direction, z, for the three regimes. Figs. 9(a), (c), and (e) show that, for the three cases, the average value of $|C_D|$ increases as L decreases, which is particularly evident for $L = 1$ (red lines). The increase in $|C_D|$ is an effect of the interaction of the bubble wake with the wall, which usually occurs in the migrating scenario established in the present work (Shi et al., 2024). This creates additional vorticity on the bubble surface due to its proximity to the wall, which induces a shear force on the bubble surface owing to the no-slip condition at the wall. The global values of $|C_D|$ are reported in Table 2. These values are similar to the stationary values $C_D^s = 4/3\,Fr^{-2}$

(also provided in Table 2). Indeed, note that C_D^s can be obtained from Eq. (7) for $U^* = v^*$, $g\cos\theta \gg C_M \mathrm{d}U^*/\mathrm{d}t^*$ and small drift angles ($\cos\theta \simeq 1$). An increase in C_D is observed for $L = 1$ of 8.3%, 5.7%, and 2.2% over $C_D(L = 4)$ for Cases 1, 2 and 3, respectively.

Drag force in the rectilinear regime: Case 1

Regarding the evolution of the local drag force, the rectilinear case (Figs 9a-b) shows a nearly constant value as the bubble rises for each value of L (see Fig. 9a). The increase in drag as L decreases persists as the bubble rises, even as it moves away from the wall. Although not shown in Fig. 9(a), the increase in drag remained even when the bubble moved vertically $z > 200$. Nevertheless, the increase in $|C_D|$ with decreasing L is not very significant, in agreement with Takemura et al. (2002), who predicted a low wall effect for $Re\,L > 10$, in the case of spherical bubbles. A detail of the evolution of $U(z)$, $\theta(z)$ and $|C_D(z)|$ over $75 \lesssim z \lesssim 95$ for $L = 1$ is shown in Fig. 9(b). In this range of z values, $|C_D(z)|$ (red) slightly decreases as the bubble rises, moving away from the wall. In addition, note that the velocity of the bubble (blue) and its inclination angle θ (black) barely change.

Drag force in the zigzagging regime: Case 2

A different scenario is observed for Cases 2 and 3, where the drag force oscillates as the bubble rises (Figs. 9c,e). If we first focus on the zigzag regime (Fig. 9c), it can be observed that after an initial transient stage ($z \lesssim 25$), $|C_D(z)|$ starts to oscillate around a mean value with nearly constant amplitude and frequency for the three values of L reported. Although the frequency does not depend on L, the mean value of $|C_D|$ and the amplitude of the oscillations increases slightly as L decreases (see Table 2). As occurs with the bubble velocity $U(z)$, $|C_D(z)|$ oscillate at a frequency twice that of the oscillations of the bubble trajectory (Shew et al., 2006; Cano-Lozano et al., 2016). In fact, $|C_D(z)|$ reaches the maximum values of oscillations when the velocity is at its minima, which occurs when $\theta = 0$ (black), that is when the velocity is vertical at the extreme positions of the zigzag. However, two different types of maxima are observed in $|C_D(z)|$, one of large amplitude occurring when the bubbles are farthest from the wall in their oscillatory motion ($z \approx 83$ and 92 in Fig. 9d) and another of smaller amplitude occurring when the bubbles are closest to the wall ($z \approx 78$ and 87 in Fig. 9c). This is because the minima of the bubble velocity are lower in the former case than in the latter. Conversely, $|C_D(z)|$ is minimum at maximum velocity, which occurs around the maximum values of θ, when the velocity vector reaches its maximum inclination. That is, $|C_D(z)|$ and $U(z)$ are in anti-phase, consistent with Eq. (7). Then, starting from the extreme positions of the zigzag trajectory, where $\theta = 0$, $|C_D(z)|$ first decreases as the bubble approaches or moves away from the wall. Both the bubble velocity and its tilt angle, θ, increase until reaching a maximum value in the middle of the bubble's excursion, when $|C_D(z)|$ hits its minimum value. From this point on, the velocity of the bubble decreases and $|C_D(z)|$ increases to a new peak when the bubble reaches its closest or furthest distance to the wall, where $\theta = 0$ and the velocity is minimum.

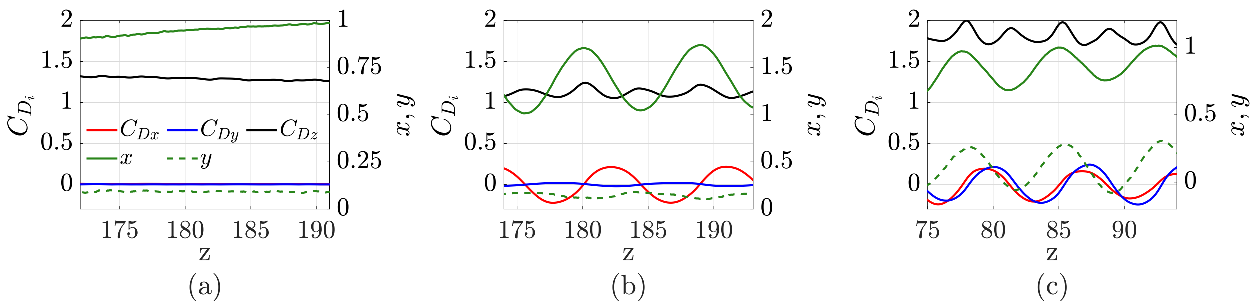

Figure 10: Components of the drag coefficient in the coordinate system (x, y, z) as a function of z (left axes), and the horizontal coordinates of the bubble centroid (right axes) for (a) rectilinear, (b) zigzag and (c) spiral regimes. Here, they correspond to the cases presented in Fig. 9 for $L = 1$ but with larger z values in (a) and (b).

Drag force in the spiralling regime: Case 3

In the spiral case (Figs. 9e,f), $|C_D(z)|$ initially increases to $|C_D| \approx 1.75$ as the instability in the bubble trajectory begins to develop. The value decreases to $|C_D| \approx 1.5$ and suddenly increases when the spiral regime is reached. The sudden increase in $|C_D|$ at $z \approx 62$ for $L =$ 1 and 2 and $z \approx 75$ for $L = 4$ corresponds to the decrease in the terminal velocity associated with a regime change, as observed in Fig. 5(b). The average value of $|C_D(z)|$ for each L, corresponding to the final stage, is given in Table 2. As observed, the increase of $|C_D(z)|$ for smaller L is not as clear as that for the other regimes. The drag force has been reported to be nearly constant in time in a spiral regime (Shew et al., 2006; Cano-Lozano et al., 2016), but $|C_D(z)|$ oscillates here because this regime is not a pure spiral but a combination with planar zigzagging. If we focus on the final stages of the bubble rise for $L = 1$ (Fig. 9f), we observe that, like in Case 2, the oscillation frequency of $|C_D(z)|$ is twice that of the bubble's path, and that $|C_D(z)|$ reaches a maximum when the velocity vector is minimum ($\theta = 0$), whereas $|C_D(z)|$ is minimum at maximum velocity and inclination. Nevertheless, in this case, both maxima of $|C_D(z)|$ have approximately the same value. As far as we are concerned, the local drag force on a bubble in this regime has not been experimentally reported before.

Components of C_D in the (x, y, z) coordinate system

Let us now analyse the components of the drag coefficient in the (x, y, z) coordinate system, as shown in Fig. 10. The horizontal components of C_D are defined as $C_{D,x} = |C_D| \sin\theta \cos(\phi + 180)$ and $C_{D,y} = |C_D| \sin\theta \sin(\phi + 180)$, while the vertical component is $C_{D,z} = |C_D| \cos\theta$. Note that $C_{D,z}$ is much larger than the horizontal components in the three regimes because the inclination of the velocity with respect to the vertical direction is small (maximum $\theta \lesssim 11°$). Indeed, in Case 1 $C_{D,x} \simeq C_{D,y} \simeq 0$ (Fig. 10a). Nevertheless, $C_{D,x}$ presents large oscillations around $C_{D,x} = 0$ in Case 2 (Fig. 10b) because the main zigzagging plane is almost perpendicular to the wall, that is, along direction $\mathbf{e_x}$, where $C_{D,y} \simeq 0$. In Case 3 (Fig. 10c), the bubble moves along both the $\mathbf{e_x}$ and $\mathbf{e_y}$ directions as it rises; hence, $C_{D,x}$ and $C_{D,y}$ exhibit oscillations of similar amplitude. Furthermore, note that $C_{D,x} > 0$ when the bubble moves closer to the wall (x decreases) and $C_{D,x} < 0$ when the bubble migrates (x decreases). In particular, $|C_{D,x}|$ is maximum at the middle of each migration and approaching stage and becomes zero when the bubble reaches its closest and furthest positions. In addition, while $C_{D,x}$ and $C_{D,y}$ vary with the frequency of the path, $C_{D,z}$ changes at twice that frequency, as C_D.

Comparison with previous results

The above description of the evolution of $C_D(z)$ is in agreement with the numerical and experimental results of recent work on bubbles rising near a vertical wall (Sugioka and Tsukada, 2015; Xiang et al., 2022; Heydari et al., 2022; Cai et al., 2023). However, each work is subject to different conditions. Therefore, a direct comparison with the present results is not appropriate. However, the global experimental $|C_D|$ reported in Table 2 can be compared with those predicted by correlations that include the effect of the initial wall distance L. Most of these correlations are valid for spherical bubbles or small deformations (Barbosa et al., 2019; Heydari et al., 2022), and may not be applicable to the cases reported in this work. Thus, we have selected just the most suitable ones to perform a qualitative comparison. For instance, the expression proposed by Fayon and Happel (1960) for solid spheres has been used in similar studies (Cai et al., 2023) to predict the increase in the drag force. It writes $C_D = C_{D,\infty} + 24/Re(K-1)$, where $K = 1/(1-1.6\lambda^{1.6})$, and λ is the ratio of the bubble diameter to the tank width, and $C_{D,\infty}$ is the drag coefficient for the unbounded case. This correlation predicts an increase in C_D of 1% for cases 1 and 2 (lower than obtained experimentally) and 3% for case 3 over C_D for $L = 4$ (assumed to be similar to the unbounded case), which is similar to our experimental result. In addition, a qualitative comparison can be made with the most recent prediction for spherical bubbles: Shi (2024) proposed an expression to calculate the increase of the drag coefficient with respect to the unbounded value for spherical bubbles given by $\Delta C_D = 0.47(2L)^{-4} + 5.5 \times 10^{-3}(2L)^{-6} Re^{3/4}$. The expression predicts a maximum increase of 3% for $L = 1$ and the current values of Re, which is fairly consistent with our experimental results, which give a maximum increase of $\simeq$ 8% over the $L = 4$ case. In any case, the influence of the initial wall separation can be incorporated into the correlations for unbounded flow via the experimental values of Re or We because both decrease with decreasing terminal velocity. A significant amount of experimental, theoretical, and numerical research is available in the literature that enables the prediction of the drag coefficient in unbounded flow. These expressions vary based on specific control parameters, applying to a specific set of conditions. In this context, expressions for spherical bubbles, such as $C_{D,L} = 48/Re$ (Levich, 1949) for large Re, or $C_{D,M} = 48/Re(1 - 2.211/Re^{1/2})$(Moore, 1959) for $Re \lesssim 50$, provide values of the drag force being much smaller than the experimental results, due to the shape of the bubbles in our work differing considerably from a sphere. The most accepted result taking into account the effect of the shape is that by Moore (1965), namely $C_{D,M^*} = 48/Re\, G(\chi)(1 - 2.21\, H(\chi)/Re^{1/2})$, where $G(\chi)$ and $H(\chi)$ are functions depending on the aspect ratio (Loth, 2008). However, C_{D,M^*} overestimates the experimental results, as shown in Table 3, since the expression does not hold for large deformations ($\chi \gtrsim 2$) or $Re > 50$. Schiller (1933) proposed a correlation

Table 3: Comparison of the drag coefficient obtained here, $C_{D,exp} = |C_D|$, with correlations in literature for unbounded flows.

Case	L	$C_{D,exp}$	C_{D,M^*}	$C_{D,SN}$	$C_{D,Tu}$	$C_{D,To}$
	1	1.29		1.41	1.36	
1	2	1.18	4	1.38	1.32	1.48
	4	1.19		1.38	1.33	
	1	1.13		1.05	1.00	
2	2	1.07	2	1.05	0.99	1.31
	4	1.06		1.03	0.99	
	1	1.83		1.14	1.08	
3	2	1.84	4	1.15	1.09	1.92
	4	1.79		1.16	1.10	

for C_D as a function of Re valid for fully contaminated spherical bubbles and $10 < Re \leq 200$, given by $C_{D,SN} = 24/Re(1 + 0.15Re^{0.687})$. As can be observed in Table 3, this prediction compared fairly well with the experimental $|C_D|$ in the rectilinear and the zigzag regimes, but yields lower values for the spiral case. A similar outcome is obtained with the expression by Turton and Levenspiel (1986), $C_{D,Tu} = 27.2/Re^{0.827} + 0.427$. This correlation fits the experimental data corresponding to spherical contaminated bubbles for $Re < 1000$ (Liu et al., 2024). The results obtained with this correlation agree with the experimental $|C_D|$ in the rectilinear and zigzag regimes, but significantly underestimate the experimental results for the spiral case (see Table 3). Finally, Tomiyama et al. (1998) proposed a simple but reliable correlation for C_D of single bubbles under a wide range of fluid properties and bubble diameters. The correlation consists of three equations, each corresponding to clean, slightly contaminated, and contaminated systems. The expression for clean bubbles, $C_{D,To} = \max\{\min[16/Re(1 + 0.15Re^{0.687}), 48/Re], 8/3Bo/(Bo + 4)\}$ gives values similar to the experimental results, as can be observed in Table 3. Exactly the same result is obtained using the equations for slightly and completely contaminated, indicating that, according to this study, contamination is not a critical parameter in our experiments. Note that $C_{D,To}$ does not capture the effect of L because its value comes from the term $8/3Bo/(Bo + 4)$, implying that Bo is the dominant parameter for highly deformed bubbles.

5.4.2. Lift force

The components of the lift coefficient were calculated using Eqs. (8) and (9). Our results indicate that the component of the lift force along direction $\mathbf{e_2}$, C_{L2}, balances the 2-component of the buoyancy force, $F^*_{L2} \simeq -F^*_{B2}$. Since $F^*_{B2} > 0$, F^*_{L2}, and hence, C_{L2} is always negative. Moreover, because $C_M U^* \mathrm{d}\phi/\mathrm{d}t^* \sin\theta \sim 10^{-4}$ m/s^2, it may be derived that $C_{L3} \ll |C_{L2}|$, and the magnitude of the lift coefficient essentially coincides with its component along axis 2, $C_L = \sqrt{C^2_{L2} + C^2_{L3}} \simeq |C_{L2}|$.

The evolution along the vertical direction of the local lift coefficient, $C_{L2}(z)$, obtained from Eq. (8) is shown in Fig. 11, where a negative value is always obtained according to our

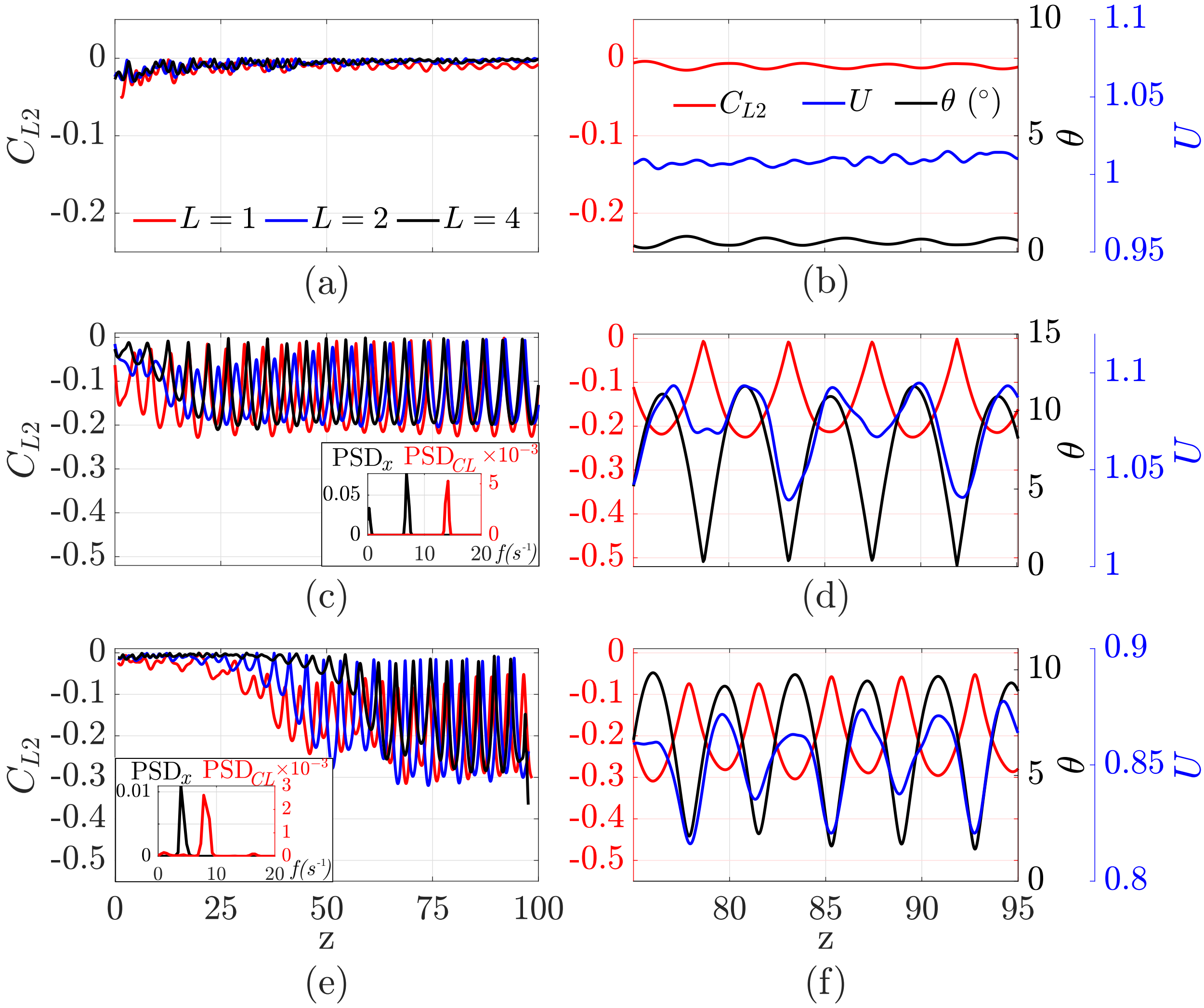

Figure 11: Evolution of the lift coefficient, C_{L2}, corresponding to experiments in the (a, b) rectilinear, (c, d) zigzagging, and (e, f) spiralling regimes, respectively. The left panels show C_{L2} for $L = 1$, 2, and 4; including an inset displaying the comparison between the power density espectrum of the oscillating trajectories and that of C_{L2}. Figures on the right show a zoom of C_{L2} (axis on the left) for $L = 1$, together with $U(z)$ and $\theta(z)$ (axes on the right in blue and black, respectively). The horizontal axes in Figures (a) and (c) are truncated to $z = 100$ for clarity.

reference frame.

Lift force in the rectilinear regime: Case 1

In the rectilinear regime (Fig. 11a,b), the lift force is nearly constant for any value of L. The average values of C_L are listed in Table 2. Note that $C_L \approx |C_{L2}|$ is very small, almost negligible for $L = 4$; however, it increases slightly as L decreases, being particularly noticeable at $L = 1$. In Fig. 11(b), corresponding to $L = 1$, we see that $C_{L2}(z)$ is always negative, keeping a low and almost constant value as z increases and the bubble moves away from the wall.

Lift force in the zigzagging and the spiralling regimes: Cases 2 and 3

In contrast, in the zigzag and spiral regimes, $C_{L2}(z)$ oscillates as the bubble rises (Fig. 11c,e). In particular, in the zigzag regime (Fig. 11c), $C_{L2}(z)$ oscillates with an amplitude that slightly increases with decreasing L. This effect is particularly evident during the first instants ($z \lesssim 10$). In addition, the permanent oscillations of $C_{L2}(z)$ are established earlier (or at lower z) as L decreases because the proximity of the wall favours the zigzag motion (Estepa-Cantero et al., 2024). Similar to the drag coefficient described above, the oscillations of $C_{L2}(z)$ are related to the zigzag motion, as can be observed in Fig.11(d) for $L = 1$, where $C_{L2}(z)$ (red) oscillates at twice the frequency of the zigzag path, as also displayed in the inset of Fig.11(c). The maximum negative value of $C_{L2}(z)$ occurs when the bubble velocity and θ are maximum, that is, when the bubble velocity reaches its maximum lateral excursion in the middle of both the migrating and approaching phases at each cycle of the zigzag motion. This result does not agree with previous studies that have predicted that the lift force varies at the frequency of the trajectory (Shew et al., 2006; Heydari et al., 2022) because, in our case, θ is defined positive. The overall evolution of $C_{L2}(z)$ in Case 3 (Figs. 11e,f) is similar to that in Case 2, but with higher amplitudes and average values (see Table 2).

Components of C_L in the coordinate system (x, y, z)

To directly relate the lift force to the wall position, the components of C_L in the coordinate system (x, y, z) are plotted in Fig. 12. The horizontal components are calculated as $C_{L,x} = C_L \cos\theta \cos\phi$ and $C_{L,y} = C_L \cos\theta \sin\phi$. Note that $C_{L,x} > 0$ when $0 \leq |\phi| < 90°$ (migration from the wall), while $C_{L,x} < 0$ when $90 < |\phi| \leq 180°$ (approximation to the wall). The vertical lift coefficient is calculated as $C_{L,z} = C_L \sin\theta$. Since $C_{L2} < 0$ and $\theta > 0$, $C_{L,z}$ is always negative, that is, the lift points towards the negative vertical direction (Fig. 12). Moreover, because the inclination of the velocity vector is always small (maximum $\theta \simeq 10°$), $C_{L,z}$ is much smaller than the horizontal components. In particular, in Case 1 (Fig. 12a), since a continuous migration motion mainly normal to the wall ($\phi \simeq 0$) occurs, $C_{L,x} > 0$ (red) and $|C_{L,y}| \simeq 0$ (blue). Thus, the lift coefficient in the wall-normal direction is positive when the bubble is repelled from the wall, in agreement with other works (Takemura and Magnaudet, 2003; Shi et al., 2020; Shi, 2024). In Case 2 (Fig. 12b), $C_{L,x} > 0$ when x (solid green line) increases, whereas $C_{L,x} < 0$ when x decreases. Therefore, $C_{L,x}$ meets previous results since it oscillates with half the frequency of the velocity oscillation, being positive (negative) when x increases (decreases). That is, the lift force is negative when the bubble approaches the wall (attractive force) and positive when the bubble migrates from the wall (repulsive force), in agreement with previous studies (Takemura and Magnaudet, 2003). Since the zigzag motion is almost normal to the wall (y barely varies), $|C_{L,y}| \ll |C_{L,x}|$. In Case 3 (Fig. 12c), the general picture is similar to that of Case 2, but now $|C_{L,y}| \sim |C_{L,x}|$ because oscillations in y are comparable to those in x. Both components are nearly in phase because x and y are also. Additionally, $C_{L,z}$ is larger than in Cases 1 and 2 and oscillates at twice the frequency of the trajectory, that is, at the frequency of the velocity or θ.

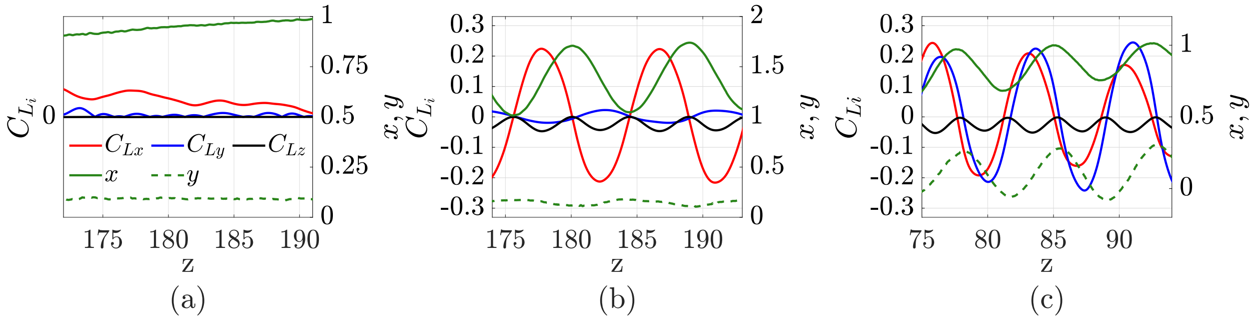

Figure 12: Components of the lift force coefficient in the coordinate system (x, y, z) as a function of z (left axes), and the horizontal coordinates of the bubble centroid (right axes) for (a) Case 1, (b) Case 2, and (3) Case 3. These correspond to the same experiments in Fig. 11 for $L = 1$ but with larger z values in (a) and (b).

Comparison with previous studies

The oscillatory behaviour of the lift force for zigzagging and spiralling paths has been reported in previous studies (Lee and Park, 2017; Zhang et al., 2020; Heydari et al., 2022; Xiang et al., 2022; Cai et al., 2023). Nevertheless, most of the latter works focus on spherical or small-Bond bubbles and usually higher Re; thus, a direct comparison of the lift force evolution is not suitable. Regarding the global values of C_L (Table 2), Cases 2 and 3 exhibit a similar value ($C_L \sim 10^{-1}$), whereas C_L is lower for Case 1 ($C_L \sim 10^{-3}$). This is in fair agreement with the experimental results of Takemura and Magnaudet (2003) for contaminated spherical bubbles, who obtained repulsive lift forces with $C_L \sim 10^{-2}$ for $Re \sim 10^2$ and $L = 1$. As for the studies on deformable bubbles, Cai et al. (2023) experimentally obtained similar values ($C_L \sim 10^{-1}$) for elliptical bubbles. Furthermore, the lift force numerically obtained by Zhang et al. (2020) for a bubble with (Bo, Ga, L)=(16, 90, 0.75) that rises in spiral regime ($F_L^* \simeq 1.2 \times 10^{-4}$ N) compares fairly well with our result for Case 3 and $L = 1$, $F_L^* = C_L \rho \pi D^2 U^{*2}/8 = 2.6 \times 10^{-4}$ N. Recently, Zhang et al. (2025) numerically obtained $C_L \simeq 10^{-1}$ for spherical bubbles in a linear shear flow at $50 \lesssim Re \lesssim 100$. Moreover, they observed that the lift force is reduced when the bubble is sufficiently deformed due to the enhancement of the S-mechanism (responsible for lift reversal) over the L-mechanism (responsible for the migration) that occurs for intermediate-to-high Re, in agreement with Adoua et al. (2009). The S and L mechanisms describe lift forces on bubbles in shear flows (Legendre and Magnaudet, 1998) while the S mechanism (Shear-induced lift) is caused by the velocity gradient, creating an asymmetric pressure distribution that pushes the bubble away from high-velocity regions; the L mechanism (Lift due to rotation) arises when the bubble rotates, generating an additional lift force similar to the Magnus effect. In particular, for bubbles of aspect ratio $\chi = 2.5$, Zhang et al. (2025) predicted $C_L \simeq 0.04$ for $Re = 50$ and $C_L \simeq 0.02$ for $Re = 100$, which are of the order of our values for Case 1, but much lower than our results for Cases 2 and 3. In any case, note that Zhang et al. (2025) considered a linear shear flow, and the flow field established between the wall and the bubbles has not

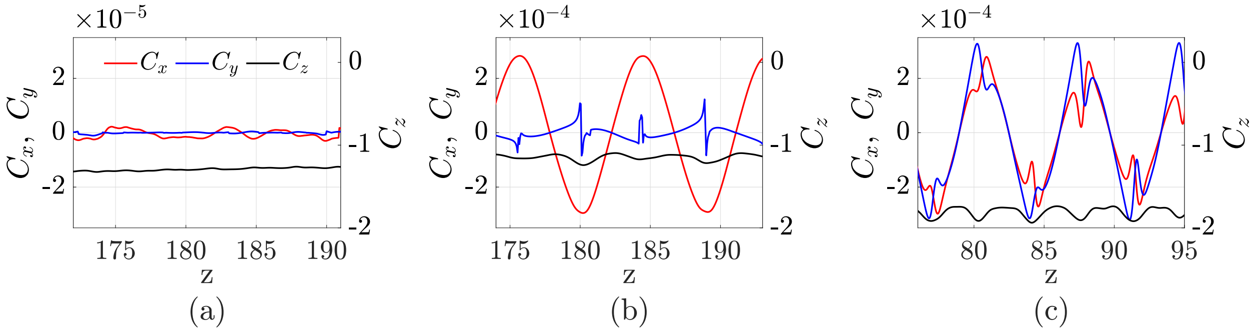

Figure 13: Evolution of the hydrodynamic force coefficients in the coordinate system (x, y, z) for (a) Case 1, (b) Case 2, and (3) Case 3 and L=1. Here, the left axes correspond to the horizontal components while the right ones show the vertical components.

been characterised in our case.

Finally, regarding the correlations for C_L, as far as we are concerned, no results in the literature predict the effect of wall separation on the lift force of deformable bubbles. Some expressions taking into account the effect of L have been developed, but only for spherical bubbles. The most recent expression that accounts for the wall effect is provided in the numerical study by Shi (2024), which is applicable to clean spherical bubbles. However, the predicted lift force is negative (attractive) within our range of L, which changes to positive (repulsive) when $L \lesssim 0.65$ for $Re = 50$ and when $L \lesssim 0.5$ for $Re = 100$, meaning that the previous numerical results cannot be applied to ellipsoidal bubbles. In relation to the correlations for the unbounded flow, some studies have considered the effect of the bubble shape on the lift force. Rastello et al. (2011) proposed an expression for C_L that corrects the value corresponding to a spherical bubble through the aspect ratio χ. However, they obtain $C_L \gtrsim 1$ in our range of parameters, which is larger than our experimental results. There are also correlations that take into account the effect of bubble deformation by Bo. For instance, in simple shear flows, Tomiyama et al. (2002) suggested $C_{L,T} = 0.00105\, Bo_T^3 - 0.0159\, Bo_T^2 - 0.0204\, Bo_T + 0.474$ for $4 < Bo_T < 10$, independent of the shear rate, with a modified Bond number based on the major axis instead of the bubble diameter, which they found a more representative length scale for the lift force ($Bo_T = \chi^{2/3} Bo$). This correlation was corrected for contaminated liquids by Hessenkemper et al. (2021). This function of Bo_T confirms a repulsive force (negative values) for our experimental cases, specifically providing an excellent agreement for Case 2 ($C_{L,T} = -0.12$). Finally, Feng and Bolotnov (2018) applied the latter correlation to a linear shear flow bounded by a wall, providing a new expression to predict the lift coefficient sign. They reported a reduced critical Bond number for the lift sign change when the wall is present; however, the estimation by Tomiyama et al. (2002) for the lift coefficient is still valid for the wall-bounded cases.

5.4.3. Total hydrodynamic forces

The components of the lift and drag forces in the coordinate system (x, y, z) were plotted together to complete the analysis of the hydrodynamic forces acting on the bubble. In particular, the components of the hydrodynamic force coefficients C_x, C_y, and C_z are presented in Fig. 13, where $C_x = C_{D,x} + C_{L,x}$, $C_y = C_{D,y} + C_{L,y}$, and $C_z = C_{D,z} + C_{L,z}$. Note that in Case 1 (Fig. 13a), the total hydrodynamic force is mainly directed in the vertical direction because the bubble velocity is predominantly vertical, with the horizontal forces being much smaller than the vertical ones ($C_x \sim C_y \sim 10^{-5} \ll |C_z| \sim 1$). Although small, the force in the normal direction of the wall is larger than that in the parallel direction to the wall ($C_x > C_y$), reflecting continuous bubble migration from the wall in the normal direction (direction $\mathbf{e_x}$). In Cases 2 and 3, C_x and C_y exhibit oscillations with amplitude $\sim 10^{-4}$. Note that $C_x \gg C_y$ in Case 2 (Fig. 13b) because the zigzag motion is mainly perpendicular to the wall, whereas in Case 3 (Fig. 13b), the oscillation amplitudes of both C_x and C_y were similar because the horizontal motion varies in both directions.

6. Conclusions

An experimental study was conducted to analyse the effect of a vertical wall on the hydrodynamic forces acting on a bubble rising near it. Three different rising regimes corresponding to high Bond numbers were investigated experimentally using various liquids and bubble sizes: one stable (rectilinear) and two unstable (zigzag and spiral), characterised by the dimensionless parameters Ga and Bo, with the resulting Re number falling in an intermediate range. For each regime, different initial distances from the wall ($L = 1$, 2, and 4) were analysed, with the $L = 4$ case behaving as an unbounded flow ($L \to \infty$). Our results indicate that the wall does not modify the bubble path instability but induces a net migration of the bubble away from it in all cases. The analysis of the evolution of the path, velocity, and orientation of the bubbles allowed for a detailed description of the bubble motion in each regime.

In the stable regime (Case 1 in table 2), the horizontal velocity normal to the wall remained low but positive because of the migration effect. The pitch angle θ is small and increases with decreasing L, caused by the enhanced lateral migration. In contrast, the azimuthal angle ϕ oscillates around zero, indicating that the horizontal displacement is mainly perpendicular to the wall and always directed away from it. Differently, fluctuations in velocity and orientation were observed in the unstable cases. In the zigzag regime (Case 2 in table 2), the bubble oscillates with a larger amplitude in the direction normal to the wall because the primary zigzag plane is nearly normal to it. The pitch angle, θ, fluctuates twice a cycle and indicates that the bubble minor axis lies vertically at the extreme positions of the zigzag motion, while its maximum inclination occurs in the middle of each migrating and approaching stage of the cycle. The azimuthal angle, ϕ, oscillates between $\pm 180°$ once per cycle, indicating abrupt bubble rotations at the transitions of both phases of the zigzag motion. Lastly, in the spiral regime (Case 3 in table 2), the oscillations in $\mathbf{e_x}$ and $\mathbf{e_y}$ directions have similar amplitudes because of the helical motion while the bubble moves away from the wall. The helical motion is also reflected in θ and ϕ. The bubble changes direction abruptly in each phase, with ϕ increasing or decreasing depending on the rotation direction.

Drag and lift forces were obtained non-invasively by applying Kirchhoff's equations to the experimental results. Specifically, bubble velocity, aspect ratio, and orientation angles are required. A coordinate system $(1, 2, 3)$ attached to the bubble was used, with $\mathbf{e_1}$ aligned with the velocity of the bubble. The alignment of the minor axis with the velocity vector was checked as a necessary condition to apply the simplified version of the Kirchhoff equations.

The drag force balances the buoyancy projection in the direction of bubble motion, since the inertia term is negligible compared to gravity. In the rectilinear case, $C_D(z)$ remained almost constant as the bubble rose. However, in unstable cases, $C_D(z)$ oscillated at twice the frequency of the bubble trajectory and peaked when the velocity was vertical ($\theta = 0$). In particular, in the spiral case, $C_D(z)$ increased sharply during regime transitions and followed an oscillatory pattern. In all regimes, the vertical drag component was greater than the horizontal due to the small angle of inclination. Nevertheless, in the unstable regimes, the horizontal components oscillate according to the bubble trajectory. The overall average drag coefficient increased when L was small due to the interaction of the bubble wake with the wall, generating additional vorticity and shear forces.

The lift force acted in the direction of the bubble velocity, with the resulting lift coefficient primarily defined by C_{L2} given that $C_{L3} \approx 0$. This indicated that the lift force compensated the buoyancy force in the direction of $\mathbf{e_2}$. In the rectilinear case, C_{L2} was almost constant and negligible for L=4 but increased slightly as L decreased. In unstable regimes, C_{L2} oscillated with larger amplitudes in the spiral regime. In particular, in the zigzag regime, C_{L2} fluctuated at twice the trajectory frequency, reaching a maximum absolute value when the bubble was at its maximum lateral deviation from the mean path. Most available correlations have been provided for spherical bubbles and do not fully capture the behaviour of deformable bubbles near a wall. However, a fair agreement was found with previous experimental and numerical results.

Acknowledgments

This work was supported by the coordinated project PID2020-115961RB-C31, PID2020-115961RB-C32, financed by MCIN/AEI/10.13039/501100011033 and by PID2023-151343NB-C32, financed by MICIU/AEI/10.13039/501100011033 and by FEDER, UE. R. Bolaños-Jiménez would like to acknowledge the University of Jaén project M.2 PDC_1484 financed by Programa Operativo FEDER Andalucía 2021-2027. C. Estepa-Cantero would like to thank the Spanish Ministry of Universities for the financial support the Fellowship FPU20/02197 provided.

Appendix A. Kirchhoff equations

The generalised Kirchhoff equations describe the linear and momentum balance of a fluid-body system and can be applied to describe the motion of a bubble that rises in a stagnant viscous liquid as follows (Mougin and Magnaudet, 2001),

$$
\begin{aligned}
(m^*\mathbb{I} + \mathbb{A}^*)\frac{\mathrm{d}\mathbf{U}^*}{\mathrm{d}t^*} + \boldsymbol{\Omega^*} \times [(m^*\mathbb{I} + \mathbb{A}^*)\mathbf{U}^*] = \mathbf{F}^* \\
(\mathbb{J}^* + \mathbb{D}^*)\frac{\mathrm{d}\boldsymbol{\Omega^*}}{\mathrm{d}t^*} + \boldsymbol{\Omega^*} \times [(\mathbb{J}^* + \mathbb{D}^*)\boldsymbol{\Omega^*}] + \mathbf{U}^* \times (\mathbb{A}^*\mathbf{U}^*) = \boldsymbol{\Gamma}^*
\end{aligned}
\tag{A.1}
$$

where m^* is the mass of the bubble, $\mathbf{\Omega^*}$ is the rotation rate of its centre of mass, $\mathbb{I}$ is the unit tensor, $\mathbb{J}^*$ is the inertia tensor of the bubble, $\mathbb{A}^*$ and $\mathbb{D}^*$ are second-order diagonal tensors characterising the mass of fluid set in motion by translation and rotation of the bubble, and $\mathbf{F}^*$ and $\mathbf{\Gamma}^*$ are the resulting hydrodynamic force and torque on the bubble, respectively. However, assuming that the bubble has zero inertia, the force and torque balances are given by Eqs. (1)-(2).

The added mass tensors $\mathbb{A}^*$ and $\mathbb{D}^*$ depend on the shape of the bubble, which we assume to be an axisymmetric ellipsoid, as also done in other studies on rising bubbles (Mougin and Magnaudet, 2001, 2002; Shew et al., 2006; Shew and Pinton, 2006; Zawala et al., 2007; Kusuno et al., 2019; Xiang et al., 2022). If Eqs. (A.1) are evaluated in an inertial frame of reference rotating with the bubble (see Fig. 1b), we may obtain a diagonal expression for these tensors,

$$\mathbb{A}^* = \begin{bmatrix} A^*_{11} & 0 & 0 \\ 0 & A^*_{22} & 0 \\ 0 & 0 & A^*_{33} \end{bmatrix}, \qquad \mathbb{D}^* = \begin{bmatrix} D^*_{11} & 0 & 0 \\ 0 & D^*_{22} & 0 \\ 0 & 0 & D^*_{33} \end{bmatrix}, \tag{A.2}$$

whose components may be derived from the expression for the kinetic energy associated with the motion of an oblate spheroidal body along its axis of symmetry in an unbounded flow, proposed by Lamb (1924); Korotkin (2008), and widely used in similar studies on rising bubbles (Tsao and Koch, 1997; Mougin and Magnaudet, 2001, 2002; Shew et al., 2006; Shew and Pinton, 2006; Zawala et al., 2007; Kusuno et al., 2019; Xiang et al., 2022):

$$\begin{gathered} A_{ii} = \rho V C_{Mi} = \rho V \frac{\gamma_i}{2-\gamma_i}, \\ \gamma_1 = \gamma_2 = \frac{1}{\chi^2-1}\left[\chi^2 - 1 + \sqrt{1-\frac{1}{\chi^2}}\chi^3 \arcsin\left(\sqrt{1-\frac{1}{\chi^2}}\right)\right] \\ \gamma_3 = \frac{2\chi^2}{\chi^2-1}\left[1 - \frac{1}{\sqrt{\chi^2-1}}\arcsin\left(\sqrt{1-\frac{1}{\chi^2}}\right)\right], \end{gathered} \tag{A.3}$$

$$\begin{gathered} D_{ii} = \rho V U^2 C_{Ti} \\ C_{T1} = C_{T2} = \frac{((\chi^2-1)^2}{\chi^2+1} \frac{(2\chi^2+1)\sqrt{1-\frac{1}{\chi^2}} - 3\chi \arcsin\left(\sqrt{1-\frac{1}{\chi^2}}\right)}{(7\chi^2-1)\sqrt{1-\frac{1}{\chi^2}} + 3(\chi^3+\chi)\arcsin\left(\sqrt{1-\frac{1}{\chi^2}}\right)} \\ C_{T_3} = 0 \end{gathered} \tag{A.4}$$

The assumption of $\beta \simeq 0$ allows us to neglect the torque balance in Eq. (A.1) and assume that the bubble velocity vector has only one component along the direction $\mathbf{e_1}$, $\mathbf{U}^* = U^*\mathbf{e_1}$. Using the latter simplifications, the force components given by the Kirchhoff equations can be written as

$$F^*_i = A^*_{ij}\frac{\mathrm{d}U^*_j}{\mathrm{d}t^*} + \epsilon_{ijk}\,\Omega^*_j\,A^*_{kl}\,U^*_l, \tag{A.5}$$

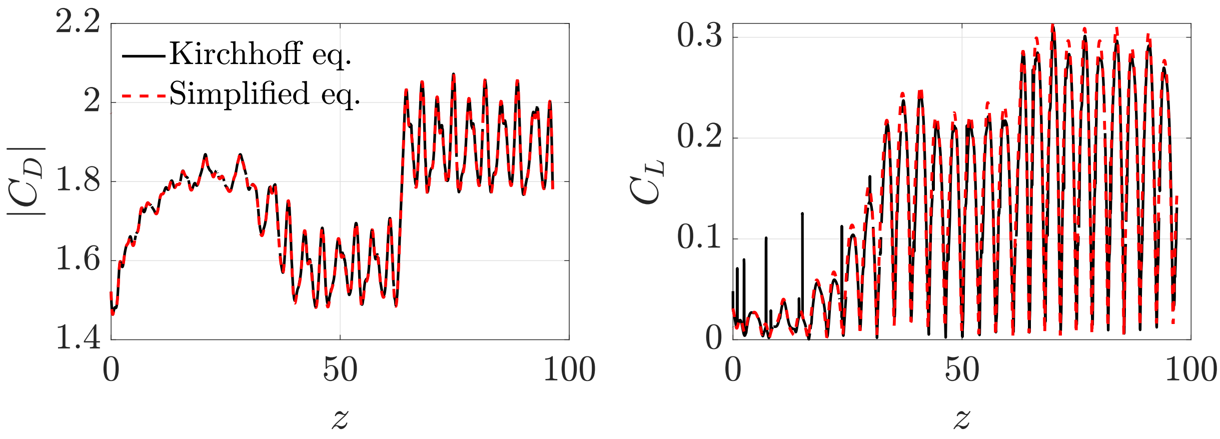

Figure A.14: Evolution of the drag and lift coefficients magnitudes for one experiment in Case 3 ($\beta(t)_{max} \approx 12^o$) calculated with the original version of the Kirchhoff equations (black, solid lines) and their simplified version (red, dashed lines).

which provides Eqs. (3), and where ϵ_{ijk} is the alternating unit tensor.

This assumption may be verified by applying the equations directly in an inertial frame of reference with origin on the bubble centroid and axes coinciding with the minor and major axes of the axisymmetric ellipsoid. As a previous step, the measured kinematic variables must be rotated from the laboratory frame of reference (x, y, z), by means of a rotation matrix R_1 based on angle α, to the inertial one (Eq. A.6),

$$R_1 = \begin{bmatrix} \cos(\alpha_{xy}) \cdot \cos(\alpha_{xz}) & 0 & 0 \\ 0 & \cos(\alpha_{xy}) \cdot \cos(\alpha_{yz}) & 0 \\ 0 & 0 & \cos(\alpha_{xz}) \cdot \cos(\alpha_{yz}) \end{bmatrix}. \tag{A.6}$$

After computing the forces and torques, the values of the drag and lift forces may be derived by rotating their components to the frame of reference $(1, 2, 3)$, which has the same centroid but it is aligned with the velocity, and thus with the drag force. This rotation (R_2) will be based on angles ϕ and θ

$$R_2 = \begin{bmatrix} \cos(\phi) \cdot \cos(\theta_{xz}) & 0 & 0 \\ 0 & \cos(\phi) \cdot \cos(\theta_{yz}) & 0 \\ 0 & 0 & \cos(\theta_{xz}) \cdot \cos(\theta_{yz}) \end{bmatrix}. \tag{A.7}$$

These expressions provide a more accurate result for both the forces and the torques. Figure A.14 shows the comparison between the force coefficient calculated from the simplified Kirchhoff equations and the full ones. To ensure the validity of the assumption $\beta = 0$, we evaluated the complete equations for the case with a maximum value of β in our set of experiments ($\beta(t)_{max} \approx 12^o$), and compared with those obtained from the simplified equations (Eqs. 7-8). It can be observed that the results are nearly identical in the drag force ($< 0.5\%$) and only small discrepancies are shown in the lift force, which displays a slight phase difference and an increment of the peak values due to the $\beta = 0$ assumption. The differences between the mean values of the lift forces obtained with the full and the simplified equations were always lower than 3.2%. Additionally, the torque evaluated with the second equation in (A.1) provides a negligible value. This proves the validity of the assumption of $\beta = 0$ and the use of the simplified version of the Kirchhoff equations, which are easier to implement.

Appendix B. Experimental details

The tank was equipped with four glass sides to ensure optical access and cleanliness, enclosed by a full methacrylate cover. Air was injected at a controlled flow rate through an injector located at the tank's base to generate bubbles. A capillary tube was placed between the injector and the air supply line to maintain a steady flow, and very low flow rates were applied to ensure quasi-static bubble formation, confirmed through high-speed video analysis. A superhydrophobic substrate (Rustoleum® NeverWet™) was used as an air injector to obtain the high-Bond number bubbles required in Case 3.

Table B.4: Main properties of the liquids

Case	Liquid	ρ (kg/m^3)	μ (mPa·s)	σ (mN/m)
1	T11 - Silicon oil	935	9.35	20.1
2	T05 - Silicon oil	913	4.57	19.7
3	Glycerol-water (GW)	1188.7±1.1	22.1±1.9	65.7±0.1

Regarding the liquids, Table B.4 lists their properties. The liquid temperature was continuously registered during the experimental runs. The liquid physical properties were measured with a Brookfield DV3TLVCJ0 rheometer, Krüss K20 tensiometer, and Mettler Toledo Density2Go densimeter, which matched theoretical data and those provided by the manufacturers. To reduce surfactant effects, the liquids were replaced periodically. Moreover, before experiments, the tank and wall were deeply cleaned with water and ethanol to remove dust and surfactants.

A THORLABS-R1L3S1P 10 *mm* Stage Micrometer with 50 μm divisions was employed as calibrating device. Images were taken at different positions in both vertical planes. Moreover, they were checked for focus depth, and the pixel-to-millimetre ratio was computed several times for statistical convergence.

Both cameras' motion, synchronised with the servomotor, was registered for every experiment. Their position together with the bubble position in the shadowgraphy images provided us with the bubble centroid position. A plumb bob ensured the wall and camera system's verticality, and its image corrected minor displacements. Bubble terminal velocity was measured before and after each experimental round. On the one side, it is required to program the servo motor (SMC Lecsa2-S4 driver, Melsoft MR Configurator) that moves both cameras. On the other side, we were able to confirm that the terminal velocity remained unchanged, and thus the effect of contamination was not important. A laser and photodiode triggered the cameras and the traverse upon bubble pinch-off. Each case was repeated at least 10 times, with sufficient time between bubbles to avoid wake interference. Except for Case 3, all experiments were highly repetitive. Although the general picture was unaltered, the particular details of Case 3 varied from one experiment to another due to the changes in ambient temperature, which resulted in variations of the liquid (GW) physical properties.

	Case	$\mathbf{x}$	$\mathbf{U}$	Volume	D	χ	C_D	C_{L2}
Absolute error	1	0.93 μm	1.37 $\mu m/s$	0.12 mm^3	7.4 μm	0.033	3.3×10^{-3}	3.6×10^{-4}
	2	0.93 μm	1.55 $\mu m/s$	0.10 mm^3	7.4 μm	0.033	3.4×10^{-3}	9.6×10^{-4}
	3	0.90 μm	1.49 $\mu m/s$	1.18 mm^3	12.7 μm	0.018	4.3×10^{-3}	1.7×10^{-3}
Relative error (%)	1	0.001%	0.001%	0.71%	0.23%	1.2%	0.2%	0.2%
	2	0.001%	0.001%	0.79%	0.26%	1.2%	0.1%	0.1%
	3	0.001%	0.001%	0.50%	0.17%	0.5%	0.6%	0.2%

Table B.5: Maximum uncertainty of experimental measurements.

Finally, the uncertainty in the measurements was taken into account to assess the limitations of the indirect variables. First, the uncertainty of the centroid position and the length of the bubbles axes were estimated following Ho (1983). The position of the motor was registered every 0.9 ms with a precision of 0.7 μm. Subsequently, the uncertainty of the direct measurements was taken into account in order to estimate the maximum propagated error in the final results, as stated in Table B.5.

References

Adoua, R., Legendre, D., Magnaudet, J., 2009. Reversal of the lift force on an oblate bubble in a weakly viscous linear shear flow. J. Fluid Mech. 628, 23–41.

Agrawal, M., Gaurav, A., Karri, B., Sahu, K.C., 2021. An experimental study of two identical air bubbles rising side-by-side in water. Phys. Fluids 33.

Aoyama, S., Hayashi, K., Hosokawa, S., Lucas, D., Tomiyama, A., 2017. Lift force acting on single bubbles in linear shear flows. Int. J. of Multiph. Flow 96, 113–122.

Barbosa, C., Legendre, D., Zenit, R., 2019. Sliding motion of a bubble against an inclined wall from moderate to high bubble Reynolds number. Phys. Rev. Fluids 4, 043602.

Blanco, A., Magnaudet, J., 1995. The structure of the axisymmetric high-Reynolds number flow around an ellipsoidal bubble of fixed shape. Phys. Fluids 7, 1265–1274.

Bonnefis, P., Fabre, D., Magnaudet, J., 2023. When, how, and why the path of an air bubble rising in pure water becomes unstable. Proc. Natl. Acad. Sci. USA. 120, e2300897120.

Bonnefis, P., Sierra-Ausin, J., Fabre, D., Magnaudet, J., 2024. Path instability of deformable bubbles rising in newtonian liquids: A linear study. J. Fluid Mech. 980, A19.

Cai, R., Ju, E., Chen, W., Sun, J., 2023. Different modes of bubble migration near a vertical wall in pure water. Korean J. Chem. Eng. 40, 67–78.

Cai, R., Sun, J., Chen, W., 2024. Near-wall bubble migration and wake structure in viscous liquids. Chem. Eng. Res. Des. 202, 414–428.

Cano-Lozano, J.C., Bohorquez, P., Martínez-Bazán, C., 2013. Wake instability of a fixed axisymmetric bubble of realistic shape. Int. J. of Multiph. Flow 51, 11–21.

Cano-Lozano, J.C., Martínez-Bazán, C., Magnaudet, J., Tchoufag, J., 2016. Paths and wakes of deformable nearly spheroidal rising bubbles close to the transition to path instability. Phys. Rev. Fluids 1, 1–30.

Cioncolini, A., Magnini, M., 2025. Solitary bubbles rising in quiescent liquids: A critical assessment of experimental data and high-fidelity numerical simulations, and performance evaluation of selected prediction methods. Phys. Fluids 37.

De Vries, A.W., Biesheuvel, A., Wijngaarden, L.V., 2002. Notes on the path and wake of a gas bubble rising in pure water. Int. J. Multiph. Flow 28, 1823–1835.

Ellingsen, K., Risso, F., 2001. On the rise of an ellipsoidal bubble in water: Oscillatory paths and liquid-induced velocity. J. Fluid Mech. 440, 235–268.

Ern, P., Risso, F., Fabre, D., Magnaudet, J., 2012. Wake-induced oscillatory paths of bodies freely rising or falling in fluids. Annu. Rev. Fluid Mech. 44, 97–121.

Estepa-Cantero, C., Martínez-Bazán, C., Bolaños-Jiménez, R., 2024. Bubble rising near a vertical wall: Experimental characterization of paths and velocity. Phys. Fluids 36.

Fayon, A., Happel, J., 1960. Effect of a cylindrical boundary on a fixed rigid sphere in a moving viscous fluid. AICHE J. 6, 55–58.

Feng, J., Bolotnov, I.A., 2018. Effect of the wall presence on the bubble interfacial forces in a shear flow field. International Journal of Multiphase Flow 99, 73–85.

Hessenkemper, H., Ziegenhein, T., Rzehak, R., Lucas, D., Tomiyama, A., 2021. Lift force coefficient of ellipsoidal single bubbles in water. International Journal of Multiphase Flow 138, 103587.

Heydari, N., Larachi, F., Taghavi, S.M., Bertrand, F., 2022. Three-dimensional analysis of the rising dynamics of individual ellipsoidal bubbles in an inclined column. Chem. Eng. Sci. 258, 117759.

Hidman, N., Ström, H., Sardina, G., Sasic, S., 2025. A comprehensive lift force model for deformable bubbles rising in moderate shear flows. International Journal of Multiphase Flow 187, 105166.

Hidman, N., Ström, H., Sasic, S., Sardina, G., 2022. The lift force on deformable and freely moving bubbles in linear shear flows. J. Fluid Mech. 952, A34.

Ho, C.S., 1983. Precision of digital vision systems. EEE Trans. Pattern Anal. Mach. Intell. PAMI-5, 593–601.

Huang, H., Shi, P., Elkina, N., Schulz, H., Zhang, J., 2025. Path of a pair of deformable bubbles rising initially in line and close to a vertical wall. Physical Review Fluids 10, 023602.

Jeong, H., Park, H., 2015. Near-wall rising behaviour of a deformable bubble at high Reynolds number. J. Fluid Mech. 771, 564–594.

Jian, Z., Xiang, S., Li, R., Jiang, Z., Qin, L., Zhang, X., 2024. Wall effect on single bubble rising in a hele–shaw cell. Phys. Fluids 36.

Kharlamov, A.A., Chára, Z., Vlasák, P., 2008. Hydraulic formulae for the added masses of an impermeable sphere moving near a plane wall. J. Eng. Math. 62, 161–172.

Klaseboer, E., Chevaillier, J.P., Maté, A., Masbernat, O., Gourdon, C., 2001. Model and experiments of a drop impinging on an immersed wall. Phys. Fluids 13, 45–57.

Korotkin, A.I., 2008. Added masses of ship structures. volume 88. Springer Science & Business Media.

Kure, I.K., Jakobsen, H.A., La Forgia, N., Solsvik, J., 2021. Experimental investigation of single bubbles rising in stagnant liquid: Statistical analysis and image processing. Phys. Fluids 33.

Kurose, R., Misumi, R., Komori, S., 2001. Drag and lift forces acting on a spherical bubble in a linear shear flow. Int. J. of Multiph. Flow 27, 1247–1258.

Kusuno, H., Yamamoto, H., Sanada, T., 2019. Lift force acting on a pair of clean bubbles rising in-line. Phys. Fluids 31.

Lamb, H., 1924. Hydrodynamics. University Press.

Lee, J., Park, H., 2017. Wake structures behind an oscillating bubble rising close to a vertical wall. Int. J. Multiph. Flow 91, 225–242.

Legendre, D., Magnaudet, J., 1998. The lift force on a spherical bubble in a viscous linear shear flow. J. Fluid Mech. 368, 81–126.

Legendre, D., Zenit, R., Velez-Cordero, J.R., 2012. On the deformation of gas bubbles in liquids. Phys.

Fluids 24, 043303.
Levich, B., 1949. Bubble motion at high Reynolds numbers. Zh. Eksp. Theoret. Fiz. 19, 18–24.
Liu, S., Yan, Q., Guo, M., Liu, C., Wang, H., Wei, W., 2024. Research of bubble motion and correction of drag coefficient in viscous oil at low Reynolds number. Phys. Fluids 36.
Loth, E., 2008. Quasi-steady shape and drag of deformable bubbles and drops. Int. J. Multiph. Flow 34, 523–546.
Magnaudet, J., 2003. Small inertial effects on a spherical bubble, drop or particle moving near a wall in a time-dependent linear flow. J. Fluid Mech. 485, 115–142.
Magnaudet, J., Eames, I., 2000. The motion of high-Reynolds-number bubbles in inhomogeneus flows. Annu. Rev. Fluid Mech. 32, 659–708.
Maxworthy, T., Gnann, C., Kürten, M., Durst, F., 1996. Experiments on the rise of air bubbles in clean viscous liquids. J. Fluid Mech. 321, 421–441.
Mikaelian, D., Larcy, A., Cockx, A., Wylock, C., Haut, B., 2015. Dynamics and morphology of single ellipsoidal bubbles in liquids. Exp. Therm. Fluid Sci. 64, 1–12.
Milne-Thomson, L., 1996. Theoretical Hydrodynamics. Dover Books on Physics Series, Dover Publications.
Moore, D., 1965. The velocity of rise of distorted gas bubbles in a liquid of small viscosity. J. Fluid Mech. 23, 749–766.
Moore, D.W., 1959. The rise of a gas bubble in a viscous liquid. J. Fluid Mech. 6, 113–130.
Mougin, G., Magnaudet, J., 2001. Path instability of a rising bubble. Phys. Rev. Lett. 88, 4.
Mougin, G., Magnaudet, J., 2002. The generalized kirchhoff equations and their application to the interaction between a rigid body and an arbitrary time-dependent viscous flow. Int. J. of Multiph. Flow 28, 1837–1851.
Mougin, G., Magnaudet, J., 2006. Wake-induced forces and torques on a zigzagging/spiralling bubble. J. Fluid Mech. 567, 185–194.
Rastello, M., Marié, J.L., Lance, M., 2011. Drag and lift forces on clean spherical and ellipsoidal bubbles in a solid-body rotating flow. J. Fluid Mech. 682, 434–459.
Rodríguez-Rodríguez, J., Sevilla, A., Martínez-Bazán, C., Gordillo, J.M., 2015. Generation of microbubbles with applications to industry and medicine. Annu. Rev. Fluid Mech. 47, 405–429.
Schiller, L., 1933. A drag coefficient correlation. Zeit. Ver. Deutsch. Ing. 77, 318–320.
Sharaf, D., Premlata, A., Tripathi, M.K., Karri, B., Sahu, K.C., 2017. Shapes and paths of an air bubble rising in quiescent liquids. Physics of Fluids 29.
Shew, W.L., Pinton, J.F., 2006. Dynamical model of bubble path instability. Phys. Rev. Lett. 97, 144508.
Shew, W.L., Poncet, S., Pinton, J.F., 2006. Force measurements on rising bubbles. J. Fluid Mech. 569, 51–60.
Shi, P., 2024. Reversal of the transverse force on a spherical bubble rising close to a vertical wall at moderate-to-high Reynolds numbers. Phys. Rev. Fluids 9, 023601.
Shi, P., Rzehak, R., Lucas, D., Magnaudet, J., 2020. Hydrodynamic forces on a clean spherical bubble translating in a wall-bounded linear shear flow. Phys. Rev. Fluids 5, 073601.
Shi, P., Tholan, V., Sommer, A.E., Heitkam, S., Eckert, K., Galvin, K., Rzehak, R., 2023. Forces on a nearly spherical bubble rising in an inclined channel flow. Int. J. Multiph. Flow 169, 104620.
Shi, P., Zhang, J., Magnaudet, J., 2024. Lateral migration and bouncing of a deformable bubble rising near a vertical wall. Part 1. Moderately inertial regimes. J. Fluid Mech. 998, A8.
Shi, P., Zhang, J., Magnaudet, J., 2025. Lateral migration and bouncing of a deformable bubble rising near a vertical wall. Part 2. Highly inertial regimes. arXiv preprint arXiv:2501.17001 .
Su, Z.Y., Sun, J., Zhang, J.W., Cai, R.Z., Sun, K.F., Chen, W.Y., Yu, C.X., 2024. Experimental investigation on dynamic characteristics of single bubble near wall in shear flow. Phys. Fluids 36.
Sugioka, K., Tsukada, T., 2015. Direct numerical simulations of drag and lift forces acting on a spherical bubble near a plane wall. Int. J. Multiph. Flow 71, 32–37.
Sugiyama, K., Takemura, F., 2010. On the lateral migration of a slightly deformed bubble rising near a vertical plane wall. J. Fluid Mech. 662, 209–231.
Takemura, F., Magnaudet, J., 2003. The transverse force on clean and contaminated bubbles rising near a vertical wall at moderate Reynolds number. J. Fluid Mech. 495, 235–253.

Takemura, F., Takagi, S., Magnaudet, J., Matsumoto, Y., 2002. Drag and lift forces on a bubble rising near a vertical wall in a viscous liquid. J. Fluid Mech. 461, 277–300.

Taylor, T.D., Acrivos, A., 1964. On the deformation and drag of a falling viscous drop at low Reynolds number. J. Fluid Mech. 18, 466–476.

Tomiyama, A., Kataoka, I., Zun, I., Sakaguchi, T., 1998. Drag coefficients of single bubbles under normal and micro gravity conditions. JSME Int. J. Ser. B 41, 472–479.

Tomiyama, A., Tamai, H., Zun, I., Hosokawa, S., 2002. Transverse migration of single bubbles in simple shear flows. Chem. Eng. Sci. 57, 1849–1858.

Tripathi, M.K., Sahu, K.C., Govindarajan, R., 2015. Dynamics of an initially spherical bubble rising in quiescent liquid. Nat. Commun. 6, 6268.

Tsao, H.K., Koch, D.L., 1997. Observations of high Reynolds number bubbles interacting with a rigid wall. Phys. Fluids 9, 44–56.

Turton, R., Levenspiel, O., 1986. A short note on the drag correlation for spheres. Powder Technol. 47, 83–86.

Xiang, S., Jian, Z., Kherbeche, A., Thoraval, M.J., 2022. Experimental study of single bubble rising near vertical wall in hele-shaw cell. Chem. Eng. Sci. 255, 117647.

Xu, W.t., Li, S.s., Pan, L.m., Li, Z.c., 2021. Experimental investigation about the lift force of a single bubble in the water at a linear shear flow. Int. J. Multiph. Flow 145, 103819.

Yan, H., Zhang, H., Liao, Y., Zhang, H., Zhou, P., Liu, L., 2022. A single bubble rising in the vicinity of a vertical wall: A numerical study based on volume of fluid method. Ocean Eng. 263, 112379.

Yan, H., Zhang, H.Y., Zhang, H.M., Liao, Y.X., Liu, L., 2023. Three-dimensional dynamics of a single bubble rising near a vertical wall: Paths and wakes. Pet. Sci. In Press.

Zand, M.K., Puttinger, S., Saeedipour, M., 2025. A new approach to unravel the lift force phenomenon of a single bubble rising in stagnant and sheared liquids. International Journal of Multiphase Flow , 105219.

Zawala, J., Dabros, T., 2013. Analysis of energy balance during collision of an air bubble with a solid wall. Phys. Fluids 25.

Zawala, J., Krasowska, M., Dabros, T., Malysa, K., 2007. Influence of bubble kinetic energy on its bouncing during collisions with various interfaces. Can. J. Chem. Eng. 85, 669–678.

Zenit, R., Magnaudet, J., 2008. Path instability of rising spheroidal air bubbles: a shape-controlled process. Phys. Fluids 20, 061702.

Zenit, R., Magnaudet, J., 2009. Measurements of the streamwise vorticity in the wake of an oscillating bubble. Int. J. Multiph. Flow 35, 195–203.

Zhang, J., Wei, B.L., Meng, W.J., Ni, M.J., 2025. Lift reversal for an oblate droplet translating in a linear shear flow: from inviscid bubble to rigid spheroid. J. Fluid Mech. 1007, A78.

Zhang, Y., Dabiri, S., Chen, K., You, Y., 2020. An initially spherical bubble rising near a vertical wall. Int. J. Heat Fluid Flow 85, 108649.

Zhu, L., Liu, L., Zhang, L., Lian, Q., Tang, S., Ma, Z., Sun, W., Pan, L., 2025. Experimental study of three-dimensional trajectory and dynamic characteristics of rising bubbles. Prog. Nucl. Energy 179, 105537.

Ziegenhein, T., Tomiyama, A., Lucas, D., 2018. A new measuring concept to determine the lift force for distorted bubbles in low morton number system: Results for air/water. International Journal of Multiphase Flow 108, 11–24.